Study of Materials Within the Interiors of Ice Giants and Sub-Neptune Exoplanets

by

Daniel Patrick Spears

A dissertation submitted in partial satisfaction of the

requirements for the degree of

Doctor of Philosophy

in

Earth and Planetary Science

in the

Graduate Division

of the

University of California, Berkeley

Committee in charge:

Professor Raymond Jeanloz, Chair

Professor Courtney Dressing

Professor Bruce Buffet

Fall 2025

Abstract

Study of Materials Within the Interiors of Ice Giants and Sub-Neptune Exoplanets

by

Daniel Patrick Spears

Doctor of Philosophy in Earth and Planetary Science

University of California, Berkeley

Professor Raymond Jeanloz, Chair

The interiors of Uranus, Neptune, and ice giant–like exoplanets remain poorly constrained, particularly regarding the high-pressure chemical processes that govern their structure, evolution, and energy balance. To address this gap, we conducted high-pressure experiments on a range “Synthetic Uranus” (water, ammonium hydroxide, and isopropanol) compositions formulated to approximate cosmic carbon, hydrogen, oxygen, and nitrogen ratios relevant to ice-giant mantles. In particular, we studied carbon-poor compositions with <10% carbon and correspondingly larger abundances of oxygen or nitrogen.

Using laser-heated diamond anvil cells with in situ X-ray diffraction and Raman spectroscopy, we observed diamond precipitation between 14 and 55 GPa at temperatures as low as 1,500 K, and for compositions with as little as ~2% carbon. These pressures, temperatures, and carbon abundances are significantly lower than reported for simpler hydrocarbon mixtures. Our results indicate that oxygen- and nitrogen-bearing species can reduce the barrier for carbon dissociation, enabling diamond formation at comparatively moderate conditions. The presence of these volatiles therefore suggests that “diamond hail” may occur at shallower depths and lower C concentrations than previously estimated, leading to consequences for internal heat transport, stratification, convective stability, and magnetic field generation. More broadly, these findings provide new constraints on the chemical pathways expected in water–ammonia–methanol–rich planetary interiors and contribute to ongoing efforts to refine evolution models for Uranus, Neptune, and analogous exoplanets.

As a secondary study, we investigated cyclohexane under dynamic compression to examine how molecular structure and hydrogen content influence hydrocarbon dissociation, carbon clustering, and metallization pathways. Cyclohexane, while not a direct compositional analog to Synthetic Uranus, serves as a clean model for isolating fundamental high-pressure reaction mechanisms that are otherwise obscured in multicomponent mixtures. We see evidence of changes in molecular structure and possible dissociation as expressed in the measured equation of state. Together, the static and dynamic results provide a more comprehensive picture

of hydrocarbon and mixed-volatile chemistry at planetary interior pressures and temperatures, informing models of material behavior across a diverse range of icy and carbon-rich worlds.

This work is dedicated to my wife who has supported me through this entire journey and has put up with all my shenanigans over the years. And to my cats who have kept me sane through my many ups and downs.

Thank you to Dr. Thomas Smart and Dr. Matthew Diamond for their help and mentorship during my PhD work. And a special thanks to Dr. Kanani K. M. Lee and Dr. Sarah Arvenson for their help in deepening my understanding of High-Pressure Mineral Physics and the use of our 4-color Laser Heating system.

Thank you to Dr. Quentin Williams at the University of California Santa Cruz Lab and the Dr. Penny Wieser Lab for their collaborations and use of their Raman systems.

Thank you for the support given to me by the NSF and NNSA. Who's support helped these experiments take place. Special thanks to Center of Materials at Atomic Pressures (CMAP) who helped in funding and travel to conduct experiments at the University of Rochester – Laboratory for Laser Energetics (LLE).

At the LLE, I would like to thank Dr. Terry-Ann Suer, Dr. Greg Tabak, and Dr. Ripp Collins for their immense help in learning how to operate and run an experiment on OMEGA EP.

Thank you to the Lawrence Berkeley National Lab – Advanced Light Source and the beamline 12.2.2 staff. Especially Dr. Martin Kunz, Dr. Bora Kalkan, and Dr. Kat Richards. Their continued help allowed for a seamless experience on 12.2.2. Additionally, thanks to Argonne National Lab for the first work done on my project. This was the moment we first made diamonds in our samples.

Table of Contents

List of Figures

List of Tables

Chapter 1. Introduction

1.1 Background and Motivation

The scientific interest in deciphering the composition, differentiation mechanisms, and internal dynamics of Uranus and Neptune motivates experimental investigation of the C-H-N-O (carbon-hydrogen-nitrogen-oxygen) system under extreme conditions. Complex C-H-N-O molecules are of interest because they are candidates for being the light elements within Earth and other planets as well. In the outer planets, like Uranus and Neptune, C-H-N-O compounds dominate the bulk of "planetary ices," a term encompassing, not just water ice (H_2O), but the broader class of volatile compounds dominant in the outer solar system, including methane (CH_4), ammonia (NH_3), hydrogen sulfide (H_2S), and nitrogen (N_2), along with their various mixtures, hydrates, clathrates, and reaction products. They also can form superionic phases, such as superionic water (Millot et al. 2019) and superionic ammonia (Robinson et al. 2017). Additionally, these compounds can be considered 'building blocks' of life, allowing for insight into organic and bio-essential materials.

Interest in Uranus and Neptune stems from their status as archetypes for a vast population of "mini-Neptune" exoplanets discovered beyond our Solar System. While the Voyager II flyby (1986 for Uranus, 1989 for Neptune) provided groundbreaking initial data on atmospheric constituents like methane, hydrogen, and helium, it yielded only indirect constraints on the deep interiors, leaving fundamental questions about their structure, composition, and thermal evolution unresolved (Stone et al., 1986; Connerney et al., 1987; Lindal et al., 1987; Sromovsky et al., 1993; Herbert et al., 1987; Ness et al., 1986, 1989; Helled et al., 2011; Podolak et al., 2019). Research on these distant worlds has been inherently limited since their discovery. Uranus, discovered in 1781, has completed only approximately 2.8 orbits of the Sun since then, while Neptune, discovered in 1846, has completed just over one full orbit. Consequently, observations capturing seasonal variations or long-term internal processes are exceedingly sparse.

The primary dataset for both planets remains the brief Voyager II encounter, supplemented by Earth-based and Hubble Space Telescope observations, which primarily probe atmospheric phenomena and cloud-top levels. Notably, both ice giants possess highly anomalous, multi-polar magnetic fields that are significantly offset from their rotational axes and geometric centers, suggesting complex dynamo processes operating within their electrically conducting, deep fluid interiors (Ness et al., 1986, 1989; Stanley & Bloxham, 2004, 2006). The limitation of Voyager II's instrumentation and current remote sensing techniques to penetrate below the cloud decks means the nature of this deep interior fluid, its composition, phase state, and role in generating the magnetic field, remains unexplored. Magnetic fields can have impact on life, interiors of planets, functions within that interior, and more. It is important to study how and why Uranus' magnetic field differs significantly from Earth's. Laboratory experiments simulating plausible interior materials and structures are therefore essential, a need further amplified by the burgeoning census of exoplanets with radii and estimated bulk densities suggesting ice giant-like compositions (Batalha et al., 2013; Fulton et al., 2017).

To interpret the limited observations on planets and connect atmospheric measurements to the behavior of the deep interior, planetary evolution models are essential. These models focus on the large-scale physicochemical processes that govern interior development, including the condensation and settling of solids from the primordial envelope, the associated convective cooling, and the long-term geochemical differentiation that shapes present-day structure and dynamics. Such processes also influence magnetic field generation and the overall thermal evolution of the planet. In addition, the high-pressure chemistry that underpins these models has broader significance, informing advances in materials synthesis, energy storage, and fundamental physics (Benedetti et al., 1999).

Despite sharing broad similarities in mass (Uranus: 14.5 $M_{\oplus}$, Neptune: 17.1 $M_{\oplus}$), radius (Uranus: 25,362 km, Neptune: 24,622 km), and inferred bulk composition (primarily "ices" and rock with a ~15-20% H/He envelope by mass), Uranus and Neptune exhibit profound differences despite both being volatile-rich sub-Neptunes. The most striking disparity lies in their magnetospheres and axial dynamics. Uranus possesses an axial tilt of 97.77°, possibly resulting from a cataclysmic giant impact causing its rotational poles to lie nearly within the ecliptic plane (Bergstralh et al., 1991; Slattery et al., 1992; Kegerreis et al., 2018). This unique orientation leads to extreme seasonal forcing and a highly asymmetric, offset magnetosphere (Ness et al., 1986). Neptune, conversely, displays significantly more vigorous atmospheric activity, featuring the fastest sustained winds in the Solar System (exceeding 2000 km/hr) and prominent, long-lived storm systems like the Great Dark Spot observed by Voyager II. Comparatively, the wind speeds of Uranus are up to 900 km/hr (Smith et al., 1989; Hammel et al., 1989, 1995). This contrast in meteorological behavior is widely attributed to fundamental differences in internal heat flow and convection dynamics; Neptune radiates approximately 2.6 times more energy than it receives from the Sun, while Uranus exhibits negligible intrinsic heat flux, suggesting a thermally quiescent or a compositionally stratified interior inhibiting large-scale convection (Pearl et al., 1990; Hammel et al., 2007).

Voyager II's reconnaissance provided measurements of bulk physical properties, mass, radius, gravitational moments, rotation periods, atmospheric composition profiles, and temperature structures, forming the initial dataset for ice giant modeling (Stone et al., 1986; Lindal et al., 1987; Connerney et al., 1987, 1991; Pearl et al., 1990). Additional analysis of the gravity fields suggests structural differences, potentially indicating distinct internal layering (Figure 1.1), composition gradients, or varying thermal histories despite their similar bulk parameters, challenging simple twin-planet models (Podolak & Helled, 2012; Nettelmann et al., 2013; Helled et al., 2020). A comparison can be seen in Figure 1.1. Currently, with the information we have we are limited in completely identifying the exact structure of Uranus and Neptune. Helled and Guillot (2018) discusses the two main models. The first, identifies layers focusing on the boundary between them; and the second, a gradient in materials and mixing between layers. The most recent Decadal Survey (National Academy of Sciences, 2023) promises new insights on the Voyager legacy combined with advanced theoretical modeling and laboratory experimentation.

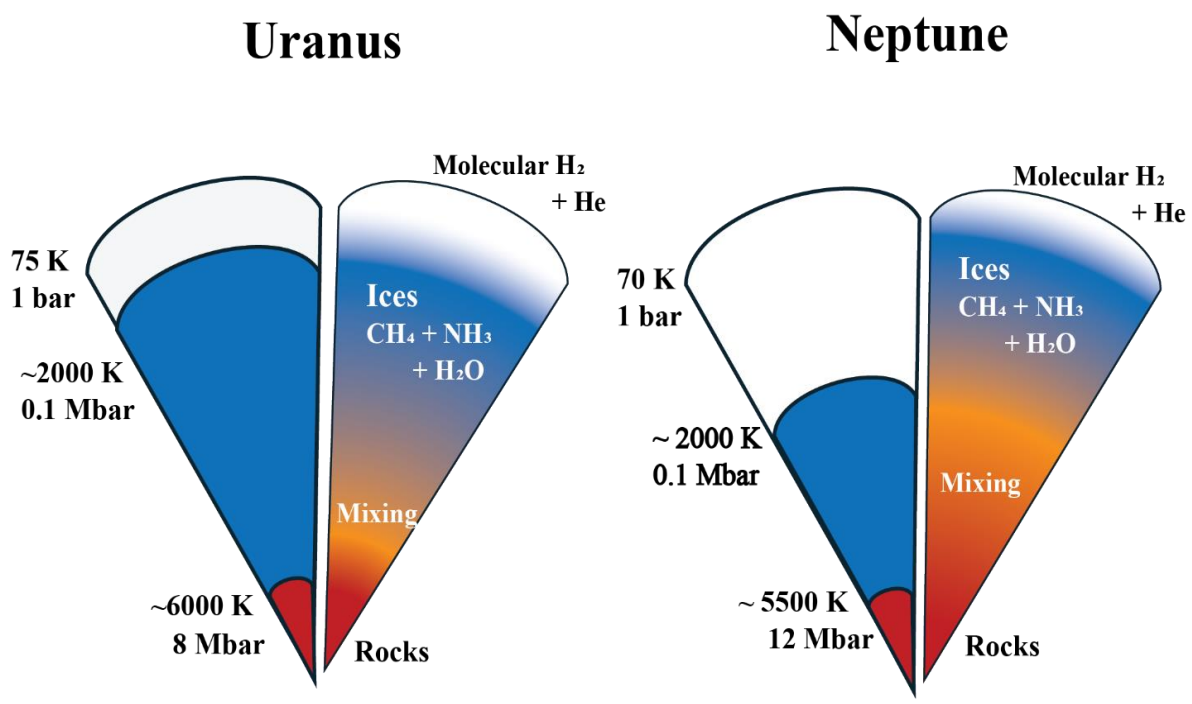

Figure 1.1 Two models for the interiors of Uranus and Neptune developed from Helled and Guillot 2018; Nettelmann et. al. 2013. The left-hand side depicts strict boundaries for compositions for each planet, but the right-hand side of each planet is the gradient and mixing model.

Since Voyager, significant progress has been made in understanding "planetary ices." Extensive research on the individual component systems (N_2, H_2, H_2O, CH_4, NH_3) under high pressure and temperature has revealed a remarkable diversity of novel crystalline and non-crystalline phases with exotic properties (Goncharov et al., 2005; Loveday & Nelmes, 2008; Somayazulu et al., 2008; Machida et al., 2008). A landmark discovery occurred in 2018 with the experimental confirmation of superionic water ice, a state in which oxygen ions form a crystalline lattice while protons diffuse like a fluid. This was achieved at pressures exceeding 100 GPa and temperatures above 2000 K, conditions directly relevant to the deep interiors of Uranus and Neptune (Millot et al., 2018). This phase, characterized by high ionic conductivity and unique mechanical properties, has profound implications for planetary magnetic field generation and heat transport.

Similarly, phases like methane monohydrate ($CH_4 \cdot H_2O$) and various high-pressure ammonia ices (e.g., ammonia dihydrate, ionic phases like ammonium hemihydrate ($NH_4^+ \cdot OH^- \cdot \frac{1}{2}H_2O$)) have been experimentally characterized (Bezacier et al., 2014; Fortes et al., 2009; Loveday & Nelmes, 2008). However, crucial gaps remain, particularly concerning the complex mixtures representative of actual planetary conditions. While theoretical studies, primarily employing ab initio molecular dynamics (AIMD) simulations based on density functional theory (DFT), have predicted a myriad of possible stable compounds, reaction pathways, and phase assemblages within the C-H-N-O system under ice giant conditions. These include exotic ionic compounds like ortho-carbonic acid (H_4CO_4), mixed molecular compounds, diamond formation, and novel clathrate structures. However, experimental validation for these

predictions, especially within multi-component systems like the "Synthetic Uranus" analog is severely lacking (Cavazzoni et al., 1999; Wilson & Militzer, 2012; Gao et al., 2010; Bethkenhagen et al., 2013, 2017; Naumova et al., 2021).

Precisely defining the ice phases, at what pressures and temperatures they are stable, reaction kinetics, and physical properties (density, conductivity, viscosity, optical spectra) are paramount as the essential starting points for planetary evolution models. This present work aims to understand planetary processes such as the condensation and precipitation of solids from the presumed mantle composition. These drive convective cooling and the geochemical differentiation of the planet's interior, influencing its current structure and dynamics. Furthermore, understanding high-pressure chemistry in these mixtures has broader applications in materials synthesis, energy storage, and in understanding how and why these Ice giant planets formed (Benedetti et al., 1999; Naumova et al., 2021).

1.2 Synthetic Planetary Ices

The concept of synthetic planetary ices emerged as a direct experimental response to Voyager II's 1986 flyby of Uranus, formalizing theoretical models of ice giant interiors. Defined as laboratory analogs simulating the dominant fluid mixtures in Uranus/Neptune mantles, these systems approximate the stoichiometry of ices (H, C, N, O) under extreme conditions, despite existing as dissociated, supercritical fluids or ionic phases at depth (Stevenson, D. J. 1985). Unlike gas giants dominated by hydrogen-helium envelopes, Uranus and Neptune possess mantles theorized to consist of fluid mixtures of H_2O, NH_3, and CH_4 at 2,000–7,000 K and 20–600 GPa, where water is the most dominant form (Hubbard et al., 1991; Nettelmann et al., 2013). To replicate compositions and environment, Nellis and colleagues pioneered the study of Synthetic Uranus: a ternary mixture of H_2O, isopropyl alcohol (C_3H_8O), and ammonium hydroxide (NH_4OH) in molar ratios (1:0.11:0.03) preserving cosmic O:C:N:H abundances (Mitchell & Nellis, 1982). Methane, which is immiscible with H_2O at ambient conditions, was substituted with isopropanol, an oxygen-poor hydrocarbon providing equivalent C:H stoichiometry (1:2.67 vs. CH_4 1:4).

Some studies, by Chau et. al. (2011), and older, have documented the electrical conductivity of Synthetic Uranus. Their electrical resistivity measurements showed an abrupt decrease when compared to individual materials, interpreted as a shift from a molecular fluid to a metastable ionic conducting state, potentially involving proton transfer or ion-pair dissociation (Nellis et. al. 1997, Chau et. al. 2011). The authors inferred carbon unmixing and diamond formation, based on carbon mass balance and shock temperature constraints, but had no direct structural evidence (e.g., x-ray diffraction) confirming diamond precipitation.

Later, dynamic compression studies extended to ~400 GPa (Sherman et al., 2012), yet static experiments have never characterized Synthetic Uranus's phase behavior at equivalent pressure and temperature conditions. Synthetic Uranus's water-rich composition (56 mol% H_2O) necessitates rigorous constraints on its H_2O-NH_3 subsystem. Ammonia depresses water's melting curve, forming low-pressure eutectics (Choukroun & Grasset, 2007), and high-pressure studies reveal ammonia hemi-hydrate II (Robinson et al., 2017) and suggest possible superionic states.

These results give insights into potential phases that could form during compression of Synthetic Uranus.

Computational efforts have attempted to resolve Synthetic Uranus's complexity. Recent ab initio molecular dynamics (AIMD) by Naumova et al. (2021) predict that ternary C-H-N-O mixtures at ~50 GPa stabilize exotic assemblages: ammonium carbamate ($NH_4CO_2^-$), polymerized hydrocarbons, and diamond in equilibrium with superionic H_2O. These simulations align with earlier Density Functional Theory – Molecular Dynamics (DFT-MD) work suggesting ionic liquid formation (e.g., [NH_4^+][$HCOO^-$]) above 10 GPa (Wilson & Militzer, 2012; Bethkenhagen et al., 2013). However, experimental validation is absent.

Studies of Synthetic Uranus can help inform models of ice giant evolution. Diamond sedimentation within the mantles of Uranus-like planets may play a role in explaining Uranus's anomalously low heat flux and suppressed convection. While sedimentation is generally associated with the release of gravitational energy, and thus heat, recent work suggests that in Uranus, the energy released by diamond formation may be offset by its sequestration in deep, stable layers, effectively insulating the interior and reducing outward heat flow (Nettelmann et al., 2016).

Additionally, chemical reactions at the interface between Synthetic Uranus-like fluids and silicate cores may produce buoyant hydrous phases, which could influence convection and thermal transport (Boujibar et al., 2020; Helled et al., 2020). Furthermore, recent modeling indicates that carbon phase separation, particularly the immiscibility between hydrocarbons and water under extreme conditions, may trap heat deep in the interior, further contributing to the low thermal emission observed from Uranus (Frost et al., 2024). In Chapter 4, we investigate these processes through room temperature and laser-heated experiments on Synthetic Uranus mixtures at pressures of 10–50 GPa and temperatures ranging from 1400 to 2000 K.

1.3 Diamond Formation in Synthetic Planetary Ices

The choice to study diamond formation experimentally comes from the proposal that diamond forms deep within the mantles of Uranus and Neptune, influencing their structural and thermal evolution (Helled et. al. 2020). Under high pressures and temperatures, carbon-rich species may dissociate and precipitate as diamonds, providing a mechanism for internal differentiation and a potential source of gravitational energy that contributes to long-term heat transport. Such diamond formation also affects the composition and properties of electrically conducting layers, with implications for convection and magnetic field generation within these planets.

The concept of diamond precipitation within the interiors of Uranus and Neptune, often referred to as "diamond rain" or "diamond hail", stands as a compelling hypothesis in high-pressure planetary science. This idea originates from early theoretical work predicting carbon phase separation under extreme pressure-temperature conditions. Ree and Ross (1992) modeled the decomposition of hydrocarbons under high-pressure conditions and predicted the potential stability of diamond, highlighting the thermodynamic instability of C–C bonds and the formation

of carbon-rich phases such as diamond. They also suggested that such phase separation could contribute to gravitational energy release, with implications for the thermal and convective behavior of ice giant interiors.

Experimental exploration of this phenomenon began with dynamic compression studies where they observed an increase in optical reflectivity above 20 GPa and 1,500 K, initially interpreted as diamond formation within an ionic fluid. However, these experiments did not provide direct structural evidence (e.g., X-Ray Diffraction or Transmission Electron Microscopy) of diamonds, and subsequent assessments have questioned whether diamond formation occurred at all. Moreover, while shock compression can probe relevant pressure-temperature regimes, it remains limited in its ability to resolve the atomic-scale mechanisms, kinetics, and structural characteristics (e.g., crystallinity or grain size) of the diamond phase.

The study of planetary carbon phases came with the application of static compression techniques. Benedetti et al. (1999) achieved the first *in situ* observation of diamond formation from a simple hydrocarbon by compressing pure methane (CH_4) in a laser-heated diamond anvil cell (DAC). This study firmly established methane as a viable diamond precursor under planetary interior conditions. However, it also raised key questions about how diamond formation would proceed in more chemically complex planetary ices, where other volatile elements, particularly oxygen and nitrogen, could alter the chemical pathways by competing for carbon atoms.

To address this, Kadobayashi et al. (2021) extended static compression experiments to multi-component carbon–oxygen–hydrogen systems relevant to Uranus, Neptune, and exoplanetary interiors. They demonstrated diamond formation from methane hydrate under pressures and temperatures relevant to ice giant interiors. Their study reveals that water-rich compositions can suppress or delay diamond precipitation, by stabilizing carbon in the form of intermediate compounds or altering phase boundaries. Their experiments also reveal that the additional presence of oxygen decreased the temperature required to form diamonds. Raman mapping revealed that diamond formation preferentially occurred at grain boundaries and interfacial regions in the solid molecular mixtures, suggesting that structural heterogeneity, such as preexisting disorder or compositional gradients, acts as a catalyst for carbon clustering and diamond formation in oxygen-rich environments.

Computational studies refine our understanding of diamond stability in planetary mixtures. Cheng et. al (2023) studied C-H mixtures computationally up to 600 GPa. However, they found that the kinetics of diamond formation were significantly suppressed when the carbon content in the mixture fell below ~15%, likely due to decreased collision rates among carbon-rich species. Bethkenhagen et al. (2017) examined various DFT calculations on H–C–O–N systems, interpreting that Neptune's mantle (~150 GPa, 7,000 K) favors diamond precipitation, whereas Uranus's cooler interior (~100 GPa, 5,000 K) could stabilize polymeric carbon chains or carbides instead. Their DFT-derived phase diagrams suggest a possible carbon-concentration threshold, where diamond becomes the thermodynamically favored allotrope only above ~10–15 mol% carbon. Below this, carbon remains dissolved in ionic fluids or forms other carbon-rich compounds. These predictions, however, remain unverified experimentally, and emerging experimental work (He et al., 2022) has begun to explore diamond formation kinetics and clustering behavior in C–H–O systems under comparable pressures. Table 1.1 presents a

comparison of computational and experimental studies done on similar materials. Using the table we can compare the atomic C% present in the mixtures examined.

Table 1.1 Comparison of previous C-H-N-O work done compared to our current study. Our study looks at an atomic concentration of carbon lower than previous studies.

Study	Mixture Studied	Study Type	Atomic %C
Cheng et. al. (2023)	CH_{16}, CH_8, CH_4, CH_2, CH, C_2H, and C_4H	Computational	6.25 – 80%
Bennedetti et. al. (1999)	CH_4	Experimental	25%
Chau et. al (2011)	Synthetic Uranus	Experimental	10%
Kadobayashi et. al. (2021)	$CH_4 \bullet H_2O$	Experimental	12.5%
He et al. (2022)	C-H-O	Experimental	23 – 71%
This study (Table 5.1)	C-Poor Synthetic Uranus	Experimental	2 – 10 %

This theoretical framework exposed a critical gap: No experimental study had quantified the minimum carbon threshold for diamond formation in ternary or quaternary systems under static compression, particularly for carbon-poor compositions (≤10%) relevant to the outer envelopes of ice giants. In this thesis, I work to characterize Synthetic Uranus and examine diamond formation in the context of carbon, oxygen, and nitrogen content. To answer questions revolving around when and what concentration of carbon is needed for formation, at what temperatures formation occurs, and what implications this can have on future understanding of ice giant interiors.

1.4 Cyclohexane

The behavior of carbon-hydrogen (C-H) systems under extreme pressure and temperature conditions is a topic of profound significance across multiple scientific disciplines, including planetary astrophysics, inertial confinement fusion (ICF), and the study of warm dense matter (WDM). Hydrogen and carbon are the first and fourth most abundant chemical elements in the universe, and their compounds dominate the interiors of ice giants like Uranus and Neptune, as well as the growing class of exoplanets known as mini-Neptunes (Hubbard W. B., 1980; Borucki et. al. 2009). Under the extreme conditions found in these planetary interiors, pressures of hundreds of GPa and temperatures of thousands of Kelvin, hydrocarbons undergo complex structural and chemical transformations, including dissociation, ionization, and metallization. These processes are critical for understanding energy and mass transport in planetary systems, as well as the thermal evolution of such bodies (Soyuer et al., 2020).

Moreover, in ICF experiments, hydrocarbons like polyethylene (CH_2) are commonly used as ablators, and their behavior under shock compression can significantly impact hydrodynamic

stability and ignition success (Orth (2016)). Thus, probing the equation of state (EOS) and phase transitions in C-H systems is essential for both fundamental science and practical applications.

Experimental and theoretical work has revealed a rich and complex phase diagram for C-H systems under warm dense matter conditions. Studies on methane (CH_4) and polyethylene have demonstrated non-linearities in the shock velocity (Us) versus particle velocity (Up). Hugoniot measurements correlate with microscopic changes such as diamond formation and hydrogen release (Tabak et al., 2024). This represents a finite volume change; that is, an abnormal compression. These features of its Hugoniot are interpreted in terms of dissociation and metallization, with reflectivity measurements providing evidence for the onset of a metallic state (Tabak et al., 2024).

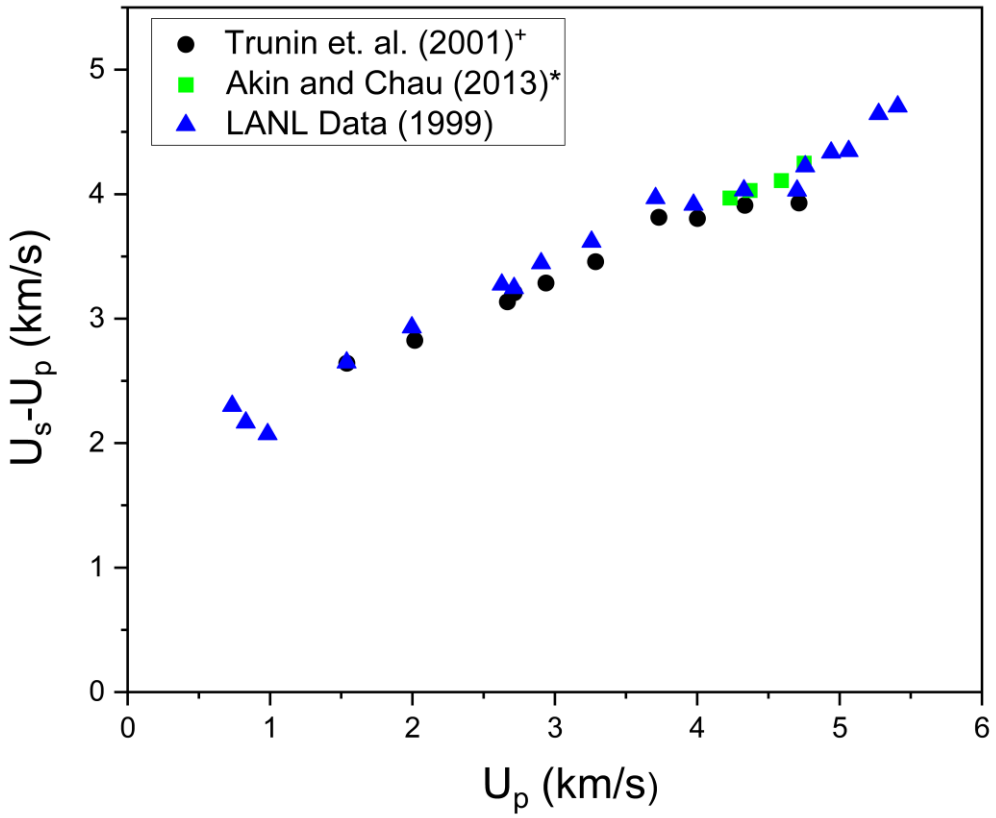

Figure 1.2. Plot of shock velocity minus particle velocity ($U_s - U_p$) versus particle velocity U_p for cyclohexane under dynamic compression. The data show a 'kink' between approximately 3.8 and 5 km/s, indicating a volume change that may result from chemical reactions or structural transformations.

The behavior of cyclic hydrocarbons, under similar conditions, remains less explored. Cyclohexane (C_6H_{12}), a saturated ring hydrocarbon, exhibits a more linear U_s-U_p relationship compared to other hydrocarbons (Ree (1979), Trunin (2001)), suggesting differences in

dissociation pathways. Figure 1.2 displays all cyclohexane data taken to date. Understanding these variations is crucial for developing a comprehensive picture of how molecular structure influences phase transitions in the C-H system under extreme compression. The scatter at the lower velocities suggests potential phase changes, or material issues.

The proposed study focuses on cyclohexane as a model system for investigating the equation of state and insulator-to-conductor transition (ICT) in hydrogen-rich carbons, including through off-principal Hugoniot compression, achieved through pre-compression in diamond anvil cells (DACs) followed by dynamic compression. Pre-compression allows access to regions of the phase diagram that are otherwise inaccessible via principal Hugoniot measurements alone, enabling a more detailed examination of dissociation and metallization thresholds (Tabak et al., 2024). Key observables include changes in U_s-U_p slopes, reflectivity, and evidence of phase separation, or diamond formation, via X-ray diffraction. Our measurements can provide critical insights into how the ring structure and high hydrogen content of cyclohexane influences its response to high compression, which is essential for refining theoretical models of planetary interiors and ICF applications.

The scientific motivation for this work is driven by recent advancements in laser-driven dynamic compression techniques (e.g., at OMEGA60, OMEGA EP, or NIF), which have enabled unprecedented access to the extreme conditions relevant to WDM. Experiments on pre-compressed methane have revealed non-linearities in the U_s-U_p relationship at particle velocities of 10–14 km/s, corresponding to pressures of 150–200 GPa and temperatures of 5,000–10,000 K (Tabak et al., 2024). However, cyclohexane's distinct molecular structure and higher hydrogen content may lead to different dissociation energetics and transition pressures. By systematically studying cyclohexane along secondary Hugoniot paths, we can determine whether its behavior aligns with existing trends or reveals new physics, such as delayed dissociation due to ring stability or unique carbon clustering mechanisms. Such insights are vital for improving the predictive capability of EOS tables like SESAME, which currently assume smooth variations for hydrocarbons (Barrios et al., 2010).

Alongside my work with planetary ices, we will discuss the preliminary results of our investigation to advance our understanding of the EOS and phase transitions in cyclohexane under extreme conditions, with implications for planetary science, ICF, and fundamental high-energy-density physics. By leveraging the unique capabilities of the Omega EP Laser Facility and combining dynamic compression with advanced diagnostics, we aim to map the mechanical and optical properties of cyclohexane along principal and precompressed-sample Hugoniot paths. Our results aim to clarify the role of molecular structure in governing dissociation and metallization processes, providing critical data to validate theoretical models and inform future experiments. This work is intended to contribute a more nuanced understanding of the behavior of hydrogen-rich hydrocarbons at extreme conditions, bridging the gap between laboratory experiments and astrophysical phenomena.

Chapter 2

Static Compression and Shock Dynamics

Models predicting diamond formation from hydrocarbon dissociation at high pressures and temperatures of ice-giant interiors underscore the need for laboratory experiments that replicate similar conditions through static compression, for example in diamond anvil cells. These measurements help define the stability and phase behavior of carbon-rich and carbon-poor mixtures, further assisting in the understanding of chemical processes operating deep within Uranus and Neptune. Dynamic compression approaches, including those using more complex hydrocarbons, such as cyclohexane, are also important because they access higher pressures and temperatures than static compression, capturing fast-reaction pathways at conditions that static methods cannot reach. By also using pre-compression, one can reach higher densities.

2.1 Static Compression

Static compression represents an experimental approach in high-pressure physics and materials science, enabling systematic investigation of material behavior under extreme pressure conditions (Bridgman P.W., 1949). Diamond anvil cells operate on the principle of uniaxial stress concentration through opposed anvil geometry. The pressure generation mechanism follows the relation presented in the equation below, where the applied force, *F,* is concentrated over the small area, *A,* of the diamond culet leading to an increase in pressure (*P)*.

$$P = \frac{F}{A}$$

This simple yet powerful design enables routine access to pressures exceeding 100 GPa, with specialized configurations, such as beveled diamonds, reaching into the tera pascal regime (O'Bannon et. al. 2018). The selection of culet diameter presents a critical optimization challenge, as smaller culets enable higher pressures but simultaneously constrain sample volume and complicate experimental measurements. For instance, a 100 μm culet diameter with 1 kN applied force generates approximately 130 GPa, though practical limitations from gasket deformation and stress distribution typically reduce this theoretical maximum. A depiction of the design of our cell is presented in Figure 3.1.

At the start of this study, particularly with our room temperature experiments, we used Merrill-Bassett cells. The Merrill-Bassett cell is a specialized adaptation of the diamond anvil concept, optimized for single-crystal X-ray diffraction studies at more moderate pressures (0-50 GPa; Merrill & Bassett, 1974). The modified geometry maximum pressure capability in exchange for improved diffraction characteristics and reduced experimental complexity. This trade-off makes the Merrill-Bassett cell particularly valuable for crystallographic investigations where extreme pressures are unnecessary (Bassett et al., 1993).

Following the initial experiments, we adopted the symmetric diamond anvil cell design for the remainder of the study. The symmetric cell is a fundamental implementation of the diamond anvil principle, optimized for superior pressure homogeneity and mechanical stability. Its design retains culet alignment under compression, which provides a more predictable and controlled pressure increment with each loading step. This design offers enhanced accuracy in pressure calibration and measurement at the cost of increased initial alignment complexity. This trade-off makes the symmetric diamond anvil cell particularly valuable for investigations requiring precise, step-wise pressure modulation and a highly uniform stress field.

Pressure determination within diamond anvil cells employs multiple complementary techniques to ensure measurement accuracy (Piermarini et al., 1975, Mao et. al. 1978). For the first half of experiments, we used ruby fluorescence to identify the pressure within our cells. Ruby fluorescence remains the most widely implemented in-situ pressure gauge, relying on the pressure-induced shift of the R_1 fluorescence line. This shift follows a well-characterized nonlinear relationship described by the following equation:

$$\mathrm{P} = \left(\frac{A}{B}\right)\left[\left(\frac{\lambda}{\lambda_0}\right)^{\mathrm{B}-1}\right]$$

Here, λ represents the measured wavelength and λ_0 denotes the ambient pressure reference (Mao et al., 1986). For quasi-hydrostatic conditions, the parameters A and B take values of 1920 GPa and 9.61 respectively (Dewaele et al., 2008). X-ray diffraction provides an independent pressure determination method through analysis of lattice parameter changes in reference materials.

The Birch-Murnaghan equation of state serves as the means for fitting high pressure compression data (Birch F., 1947). Raman spectroscopy offers additional verification through monitoring pressure-sensitive vibrational modes, though this method generally provides secondary confirmation rather than primary pressure calibration (Sharma et al., 1985). In the latter half of experiments, where we began laser heating, we decided to use the metal needed to couple with the laser as the pressure determining material. We focused on Gold and Platinum as our pressure-calibration metals. These metals were chosen due to their well characterized equations of state and their known use as a coupling material for laser heating.

Static compression techniques, such as diamond anvil cell (DAC) experiments, face inherent limitations that influence their experimental applicability (Jayaraman, A., 1983). One major constraint is the small sample volume, typically 10s to 100s of μm. This restriction complicates measurements of bulk material properties, as the sampled region may not fully represent the behavior of a larger, homogeneous system. Additionally, pressure gradients and non-hydrostatic stress conditions introduce experimental uncertainties, particularly when solid pressure-transmitting media (e.g., NaCl or Al_2O_3) are used instead of hydrostatic fluids (Bell & Mao, 1981). Non-uniform stress distributions can lead to anisotropic compression, distorting structural and electronic property measurements. These effects are especially problematic for

studies requiring precise determination of material equations of state or elastic constants. A feature is the long potential time scales of experiments, typically up to 10s of seconds, minutes, hours, or longer.

While static compression excels at achieving sustained high pressures, it is well suited for capturing fast dynamic processes, such as rapid phase transformations or metastable state formation. These complementary strengths and weaknesses guide experimental design decisions in high-pressure research, with optimal choice depending on the specific scientific objectives and required pressure conditions. Dynamic compression is most used for higher pressures than static, for example 100s of GPa versus less than 100 GPa the pressures are calculated absolutely with no need for ruby or pressure scale.

2.2 Shock Dynamic Compression

Dynamic compression is an experimental technique used to study the behavior of materials under extreme pressure and temperature conditions, typically achieved through the propagation of externally induced shock waves (i.e lasers, gas guns, explosive pads). The theoretical framework governing shock compression is derived from the conservation laws of mass, momentum, and energy, collectively known as the Rankine-Hugoniot equations. These equations describe the discontinuous changes in material properties across a shock front and are essential for interpreting high-pressure experiments. The conservation of mass is expressed as:

$$\rho_0 U_s = \rho_1 (U_s - U_p)$$

Where ρ_0 and ρ_1 are the initial and compressed densities, $U_s$is the shock velocity, and U_p is the particle velocity behind the shock. The conservation of momentum is given by:

$$P_1 - P_0 = \rho_0 U_s U_p$$

Where P_0 and P_1 represent the initial and shocked pressures. Finally, the conservation of energy across the shock front is described by:

$$E_1 - E_0 = \frac{1}{2}(P_1 + P_0)\left(\frac{1}{\rho_0} - \frac{1}{\rho_1}\right)$$

Where E_0 and E_1 denote the specific internal energies before and after compression. These equations form the basis for constructing the Hugoniot curve, which characterizes the thermodynamic states achievable under shock loading (Zel'dovich & Raizer, 2002).

The Hugoniot curve represents the end states of a material following shock compression and is typically expressed in terms of shock velocity (U_s) and particle velocity (U_p). For many materials, a linear relationship exists between these velocities:

$$U_s = c_0 + sU_p$$

where C_0 is the bulk sound speed at ambient conditions, and S is an empirically determined slope. This linear approximation has been validated for a wide range of solids, liquids, and gases. Combining this with the conservation equations allows the derivation of the pressure-density Hugoniot:

$$P_1 = \rho_0 C_0^2 \frac{\eta}{(1 - S\eta)^2}$$

Where $\eta = 1 - \rho_0/\rho_1$ is the compression ratio. Deviations from this linear behavior occur wherever there is an anomalous volume change, for example due to phase transitions, significant chemical reactions, or loss of strength (Zel'dovich and Raizer, 2002).

Precompression involves subjecting a material to an initial pressure prior to dynamic loading, shifting its Hugoniot curve to higher densities (Jeanloz et al., 2007). This approach is useful for replicating extreme conditions akin to planetary interiors, where materials are naturally compressed under immense pressures (McWilliams et al., 2012), or for accessing high-pressure states of matter, such as metallic hydrogen or exotic mineral phases, that cannot be achieved through dynamic loading alone.

The modified Hugoniot relations for a pre-compressed material must account for its initial compressed state, meaning the reference density (ρ_0), pressure (P_0), and internal energy (E_0) are those of the pre-compressed material rather than its ambient conditions (Jeanloz et al., 2007). This approach has been successfully applied in studies of hydrogen metallization (where hydrogen transitions into a conductive metal-like state at high pressures; Celliers et al., 2018, high-pressure ice phases (such as those thought to exist in icy moons like Europa; Millot et al., 2019), and the behavior of silicate minerals (e.g., quartz) at pressures comparable to Earth's core-mantle boundary (Brygoo et al., 2015). The present study uses pre-compressed states of cyclohexane for shock experiments.

Despite its utility, dynamic compression experiments face several limitations. The extremely short timescales (nanoseconds to microseconds) complicate the acquisition of high-fidelity data, necessitating advanced diagnostics such as ultrafast X-ray diffraction and velocimetry techniques (e.g., VISAR; Barker & Hollenbach, 1972). Because shock waves are inherently non-isentropic, temperature and other thermodynamic quantities must often be inferred rather than measured directly, introducing uncertainties in the derived pressure–volume–temperature (P-V-T) equations of state. Furthermore, material-specific phenomena, such as elastic-plastic transitions, fracture, and chemical reactions, can produce deviations from ideal hydrodynamic behavior (Remington et al., 2006). Nonetheless, dynamic compression remains a powerful tool for probing material behavior at extreme pressures and temperatures that static compression cannot reach.

Chapter 3

Experimental Design and Diagnostics

To investigate the high-pressure chemical pathways that may lead to diamond formation within ice-giant interiors, we designed a set of laboratory experiments that replicate relevant pressure–temperature conditions using static compression techniques. Static compression provides a foundation for understanding how carbon, nitrogen, and oxygen interact under deep-mantle conditions. Building on this framework, multiple samples of "Synthetic Uranus", and similar mixtures, are examined to document how variations in elemental ratios influence carbon-bearing phase stability at high pressure. Additionally, I conducted dynamic compression experiments on cyclohexane, a simple hydrocarbon selected for its well-defined molecular structure and relevance to carbon-rich chemistry.

3.1 Synthetic Planetary Ices (Synthetic Uranus)

3.1.1 Methodology

This experimental approach begins with the synthesis of Synthetic Uranus mixtures, following protocols established by Nellis (1987, 1988) with modifications to explore varying elemental ratios. The base Synthetic Uranus mixture consists of water (H_2O, 2.854 ± 0.03 g), ammonium hydroxide (NH_4OH, 29wt. % NH_3, *Alfa Aesar,* 3.348 ± 0.015 g), and isopropanol (C_3H_8O, *Alfa Aesar,* 3.798 ± 0.02 g). Due to the volatility of ammonia and isopropanol, fresh batches are prepared for each of our experiments to ensure compositional consistency. For Synthetic Uranus mixtures, the composition of each mixture is formulated to systematically vary the molar ratios of carbon, nitrogen, and oxygen (Tables 4.1, 5.1). For the mixtures CPA – CPC ("carbon poor"), they represent adjustments in isopropanol content to modulate carbon concentration, while ORD–ORF ("oxygen-rich") are designed as oxygen-enriched mixtures by altering the proportions of water and isopropanol. Columns NRG and NRH ("nitrogen-rich G/H") feature reduced carbon and elevated nitrogen concentrations, achieved by modifying the ammonium hydroxide and isopropanol quantities. These variations allow for a controlled investigation of the effects of elemental composition on high-pressure phase behavior for carbon-poor samples.

High-pressure experiments were conducted at Argonne National Laboratory's APS HPCAT 16-IDB beamline and Lawrence Berkeley National Laboratory's (LBNL) 12.2.2 beamline. Samples were loaded into rhenium-gasketed diamond anvil cells (DACs) with culet diameters ranging from 200 to 500 μm, and sample chambers were drilled to approximately one-third of the culet diameter (70–170 μm). Figure 3.1 depicts a schematic cross section of our DAC. Prior to compression, each sample was pre-compressed to pressures between 1 and 5 GPa, with pressure calibration performed using X-ray diffraction peaks from a metal standard (Pt or

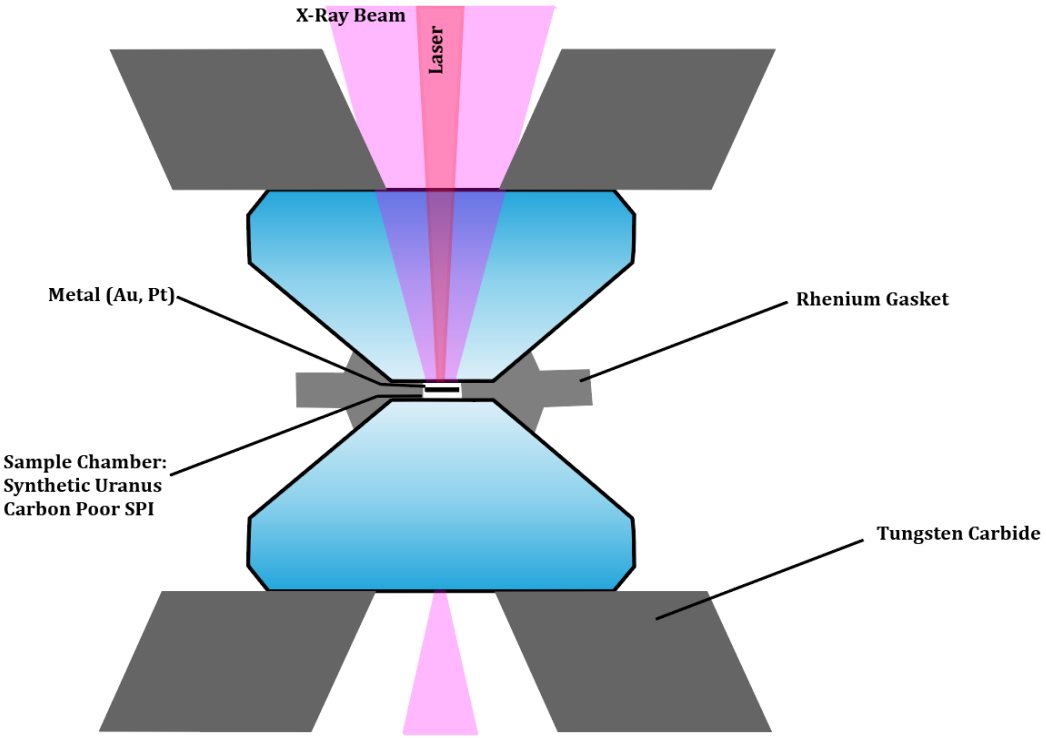

Figure 3.1. Schematic of the diamond anvil cell (DAC) used in this study. The sample chamber, located between the culets of opposing diamond anvils, was loaded with a clear liquid mixture, either Synthetic Uranus or a Carbon-Poor Synthetic Planetary Ice (SPI) mixture, depending on the experiment. The cell was designed for both room-temperature and laser-heated compression experiments, enabling investigation of phase behavior for pressures and temperatures exceeding 50 GPa and 2000 K.

Au) placed within the sample chamber. The same metal standard also served as a laser coupler during subsequent heating. In situ X-ray diffraction data were collected at specific wavelengths across the range of $\lambda = 0.4945–0.5391$ Å, with measurements taken during compression, decompression, and before and after double-sided laser heating. Temperature monitoring was achieved via spectroradiometry, ensuring thermal control during phase transitions (Kunz et. al., 2018).

Following high-pressure treatment, samples were characterized using Raman spectroscopy to identify vibrational modes: specifically, for evidence of diamond formation in carbon-poor mixtures. Room-temperature Raman measurements were performed using a Horiba LabRAM HR spectrometer by collaborators at the University of California, Santa Cruz,

employing a 532 nm laser for excitation. Additional post-experiment characterization was conducted at University of California Berkeley, Dr. Penny Weiser Lab, using a WiTec Alpha 300R Raman system, which featured a solid-state 532 nm laser with in-fiber power adjustments below 0.1 mW for enhanced sensitivity. Raman spectroscopy allowed for secondary identification of diamond formation post laser heating.

3.1.2 Analysis

Analysis of X-ray diffraction (XRD) data was performed using Dioptas (Prescher & Prakapenka, 2015)**,** a software tool designed for real-time visualization and processing of diffraction patterns. Peak identification was accomplished by referencing standard crystallographic databases (JCPDS files obtained by the LBNL ALS), enabling direct comparison with known phases from prior studies. Following initial peak matching, quantitative structural refinement was conducted via Rietveld analysis, implemented through a custom Igor Pro script. This approach allowed for precise determination of lattice parameters, phase fractions, and microstructural properties under high-pressure conditions.

Pressure calibration is achieved using equations of state (EOS) for three internal standards: platinum (Pt), gold (Au), and Ice VII. Each standard's equation of state (Holmes at al. (1989); Anderson et al. (1989); Klotz et al. (2017)) provides a reference for converting measured lattice parameters into pressure values. By cross-referencing multiple EOS models, systematic uncertainties can be estimated, toward achieving accuracy in pressure determination across the experimental range of pressures. This combined methodology, integrating Dioptas for visualization, Igor Pro for Rietveld refinement, and EOS calculations, gave a reproducible framework for characterizing various phases through changes in pressure and temperature.

3.2 Cyclohexane

To extend our understanding of carbon-rich planetary materials under extreme conditions, we performed a separate set of experiments using cyclohexane (C_6H_{12}) as a simplified, hydrocarbon-rich analog of C-H materials. Unlike the multicomponent mixtures used in Synthetic Uranus studies, cyclohexane provides a well-defined molecular structure composed solely of carbon and hydrogen, offering a clean system for probing hydrocarbon breakdown and diamond formation mechanisms. Our experimental approach combined static precompression using diamond anvil cells (DACs) with laser-driven dynamic compression, allowing us to explore high-pressure, high-temperature conditions relevant to the interiors of planets. Compared to the Hugoniot, precompression prior to shock loading places samples on lower-entropy thermodynamic paths, reducing shock heating and enabling access to denser, more planetary-relevant states. This dual-stage technique is now widely adopted in high-pressure research and is well-suited for cyclohexane due to its low initial density and sensitivity to thermal decomposition (Millot et al., 2019; Jeanloz et al., 2007). The following sections detail the target design, diagnostic setup, and shock velocity measurements used in this experimental campaign.

3.2.1 Target Design

In this work, both diamond and sapphire anvils were used as precompression DACs. Diamond anvils were used for their exceptional strength and optical transparency, while sapphires were used for their greater bandgap, which reduces susceptibility to laser-induced ionization, while also preserving the integrity of diagnostics. To prepare targets, the drive-side anvil was coated with a thin gold layer to act as an X-ray shield, and a parylene (CH) layer served as an ablator to efficiently launch shock waves. The Velocity Interferometer for any Reflector (VISAR)-side anvils were anti-reflection coated to optimize signal collection. These anvils and their coatings are destroyed in each shot.

Quartz was chosen as the impedance-matching standard in our experiments due to its well-characterized Hugoniot and favorable shock impedance properties, which lie between those of diamond and the sample materials considered here (Brygoo et. al. 2015). This intermediate impedance leads to precise impedance matching and accurate determination of shock states,

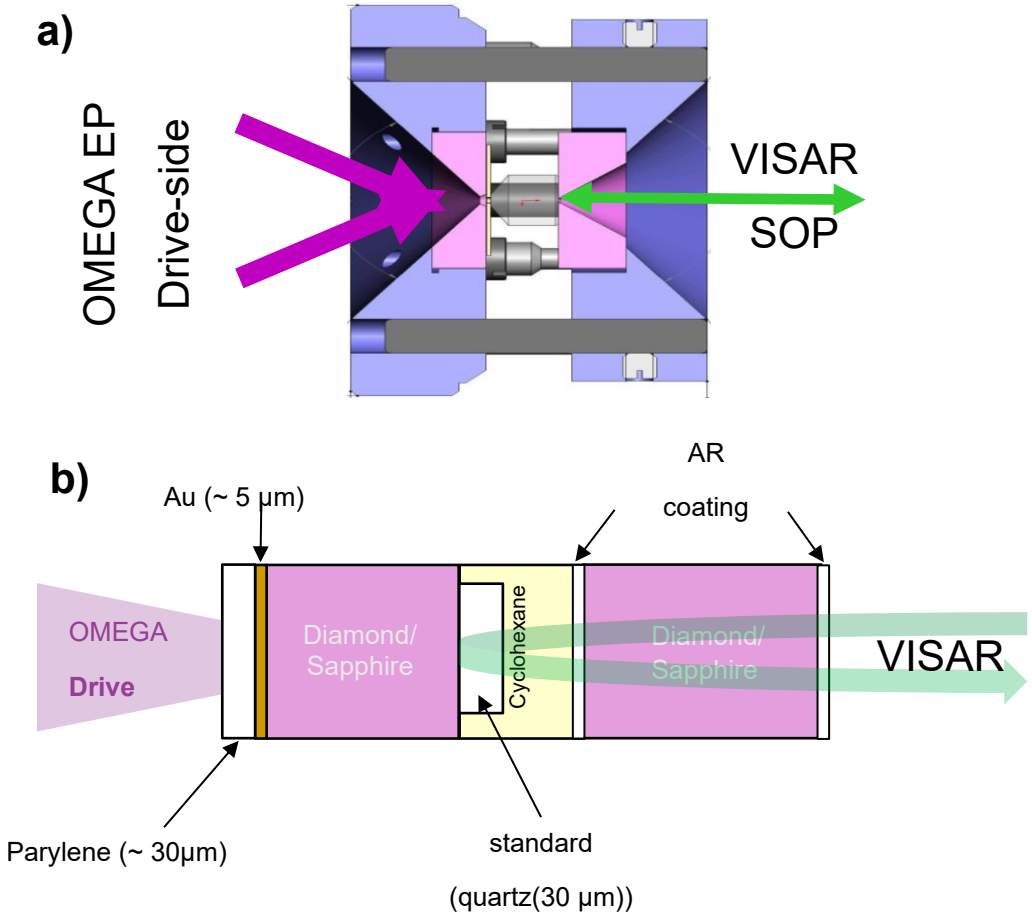

Figure 3.2. (a) Schematic of the diamond anvil cell holding the cyclohexane target. (b) Target design with our CH coating (parylene), gold coating, diamond or sapphire anvils, quartz standard, sample, and AR coatings. VISAR is the Velocity Interferometer System at Any Reflector and SOP is the streak optical pyrometer.

especially at pressures exceeding 100 GPa (1 Mbar) where quartz exhibits a strong reflective shock front critical for VISAR measurements.

Brygoo et al. (2015) highlight the advantages of quartz over diamond as a standard, noting that diamond's high stiffness and nonlinear equation of state complicate shock state analysis and introduce larger uncertainties. Quartz, in contrast, provides more reproducible and interpretable results, particularly when combined with transparent samples or multiple interface configurations, improving overall data reliability.

Furthermore, as emphasized by Jeanloz et. al. (2007), the use of precompressed samples in combination with quartz impedance matching allows access to higher density states with lower entropy generation, enabling exploration of conditions more representative of planetary interiors. This combined approach enhances the accuracy of pressure and density measurements in dynamic compression experiments, contributing to a more comprehensive understanding of material behavior under extreme conditions. Figure 3.2 presents the complete target setup, incorporating all elements discussed above, and it illustrates how this design's features work together to achieve precise control over initial experimental conditions.

3.2.2 Velocity Interferometer System for Any Reflector (VISAR)

The Velocity Interferometer System for Any Reflector (VISAR) was used to measure transient shock and particle velocities in dynamically compressed samples. The optical setup, illustrated in Figure 3.3, consists of a laser source (typically a continuous-wave Nd:YAG at 532 nm), beam splitters, delay optics, and a high-speed photo detector. The probe beam reflects off the moving sample or shock surface, and the Doppler-shifted light interferes with a reference beam delayed by a known time via an etalon delay leg. This delay converts time-dependent velocity changes into phase shifts in the interference fringe pattern, which are given as a function of time (Barker & Hollenbach, 1972; Dolan, 2006).

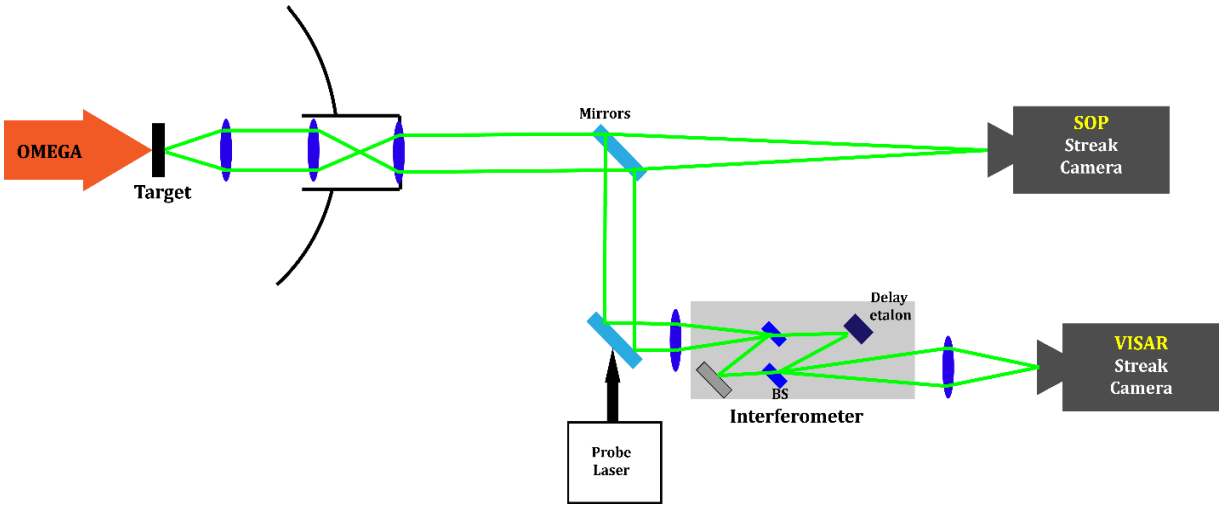

Figure 3.3. Schematic of the VISAR and SOP system at the Laboratory for Laser Energetics. Based off the schematic presented by the Laboratory for Laser Energetics (Omega Facility User Guide, Ch. 5).

To ensure accurate velocity measurements, the interferometer's delay leg is calibrated using a static mirror to determine the fringe constant, defined as $V = \lambda/2\tau$, where λ is the laser wavelength and τ is the optical delay. This constant relates observed fringe shifts to particle or shock-front velocity. Reference interferograms are recorded prior to dynamic experiments to correct for static optical path differences.

Sample alignment is important for ensuring a normal incidence of the probe beam. This minimizes wavefront distortions and maximizes signal quality. For the experiments discussed here, the VISAR system was operated in conjunction with a Streak Optical Pyrometer (SOP), discussed in the next section, enabling simultaneous acquisition of velocity and thermal emission data for time-resolved, multi-parameter diagnostics (Celliers et al., 2004).

3.2.3 Streaked Optical Pyrometer (SOP)

Complementing VISAR velocity measurements, the Streaked Optical Pyrometer (SOP) provides time-resolved thermal emission data used to estimate sample temperature during shock compression. The SOP system, also depicted in Figure 3.3, collects emitted radiation from the shocked surface and directs it through a narrowband filter (e.g., 700 ± 10 nm) or diffraction grating. The filtered light is dispersed spectrally and recorded with a streak camera, yielding temporally and spectrally resolved intensity data (Gregor, M. C., 2016).

Sample temperature is calculated by fitting the measured spectral radiance to the grey-body approximation of Planck's law:

$$I(\lambda, t) = \epsilon(\lambda) * \frac{2hc^2}{\lambda^5}\left[\exp\left(\frac{hc}{\lambda k_B T(t)}\right) - 1\right]^{-1}$$

where $\epsilon(\lambda)$ is the wavelength-dependent emissivity, and h, c, and k_B are Planck's constant, the speed of light, and Boltzmann's constant, respectively. The grey-body model accounts for the fact that real materials typically do not radiate as perfect blackbodies. Emissivity corrections are applied using available literature values or experimentally constrained estimates ($\varepsilon = 1 - R$) for the sample or window material.

SOP and VISAR measurements are synchronized temporally to allow direct correlation between temperature spikes and mechanical phenomena such as shock arrivals, phase transitions, or melting events. This combined diagnostic capability is essential for characterizing dynamic processes in high-pressure experiments. The accuracy of SOP measurements relies on a calibration against a known reference blackbody, such as a tungsten ribbon lamp, and correction for the system's spectral response (Gregor et. al., 2016).

Primary sources of uncertainty included assumptions about emissivity (typically ±5–10% in brightness temperature; Gregor et. al. 2016), detector nonlinearity, and the system's temporal resolution, which is typically on the order of 2–5 ns. In experiments using transparent windows such as LiF, isolating the sample's thermal emission is important. This is often accomplished through spatial masking of the window–sample interface to prevent window emission from biasing the measurement. For example, Seifter & Swift (2007) models the interface radiance which can be used to extract the sample temperature. Temporal resolution is provided by streak cameras or fast-gated detectors, which typically integrate over sweep windows of only a few nanoseconds, allowing temperature evolution to be resolved on shock-compression timescales.

Chapter 4

Diamond Formation in Synthetic Uranus

4.1 Introduction

Water (H_2O), ammonia (NH_3), and methane (CH_4) are key components of the mantles of Uranus and Neptune, where they form a class of materials known as planetary “ices” (Hubbard et al., 1991; Guillot & Gautier, 2014). In planetary science, “ice” refers not only to solid phases but also to the high-pressure fluid and superionic phases these materials can adopt under extreme pressure–temperature conditions (Redmer et al., 2011). At pressures reaching and exceeding 100 GPa and temperatures of several thousand kelvin, these compounds undergo complex phase transitions and chemical reactions, including dissociation and mixing with heavier elements (Lorenzen et al., 2014).

One such ice combination is “Synthetic Uranus", a water (H_2O), ammonium hydroxide (NH_4OH), and isopropyl alcohol (C_3H_8O) mixture with a C:H:N:O ratio of 4:28:1:7. This composition was chosen because of how closely it resembles the cosmo-chemical ratios for C:O (4:7), N:O (7:1), and an O:H ratio of 1:3, resulting in mole fractions of 0.71 (H_2O), 0.14 (NH_3), and 0.15 (CH_4) (Nellis et al, 1988) for the components.

The structures of Uranus and Neptune’s interiors are modeled through measurements gathered primarily by the Voyager 2 mission, including their masses, rotational velocities, radii, and gravitational fields. The atmospheric compositions consist mostly of molecular hydrogen (H_2) and helium (He). These compositions are determined via remote sensing techniques such as radio and infrared occultation and spectroscopic observations (Lindal et al., 1987). According to interior models by Guillot & Gautier (2014), the atmospheres of Uranus and Neptune are enriched in heavy elements, as evidenced by their bulk hydrogen and helium mass fractions of approximately, (0.74:0.26) and (0.71:0.29), respectively. Uncertainties arise from assumptions about cloud opacities, temperature gradients, and limited spatial resolution. The outer atmospheres extend to pressures of ~1–10 bar (0.1–1 MPa), with temperatures ranging from ~70–100 K.

Beneath these layers, pressures are estimated to reach pressures of ~2 TPa (center of planet; de Pater, I. & Lissauer, J. (2014) Table 6.1), and temperatures between 2000–7000 K (Guillot, 1999; Helled & Fortney, 2020). The mantle consists predominantly of a hot, dense mixture of water (H_2O), ammonia (NH_3), and methane (CH_4) ices in a supercritical state. At the center, a dense rocky and metallic core is present, with estimated pressures exceeding ~700 GPa and temperatures above 5000 K (de Pater, I. & Lissauer, J. (2014) Table 6.1). However, the deep interiors remain poorly constrained in terms of exact composition and the nature of layer boundaries, as Voyager 2 remains the only spacecraft to have gathered in situ data. This lack of

direct measurements has led to ongoing debates about whether their internal structures exhibit distinct compositional boundaries, gradual gradients, or a combination of both (Figure 1.1; Helled et al., 2011; Helled & Fortney, 2020; Nellis, 1988).

Thermal observations show a difference between Uranus and Neptune. Neptune emits about 2.6 times more energy than it receives from the Sun, whereas Uranus is nearly in thermal balance (Pearl et al., 1990; Pearl & Conrath, 1991). One explanation is that Neptune transports heat more efficiently through convection, with dense phases, like diamond, settling toward the core and releasing latent heat in the process (Guillot & Gautier, 2014). As diamonds sink, they both reshape mantle stratification and release gravitational energy as heat through viscous dissipation (Ross, M., 1981; Ancilotto, F. et. al., 1997; Benedetti et al., 1999).

Experimental and theoretical work has characterized the high-pressure behavior of Synthetic Uranus compositions (H_2O-NH_3-CH_4 mixtures) under dynamic compression. Nellis et al. (1997) performed gas-gun experiments on Synthetic Uranus, measuring electrical conductivity via *in-situ* four-probe techniques at 40-70 GPa and 2000-4000 K. They observed a discontinuous increase in conductivity to ~100 S/m above 30 GPa, corresponding to molecular dissociation and the onset of ionic conduction. Complementary work by Chau et al. (2011), using laser-shocked ices containing 5% CH_4, demonstrated carbon precipitation above 150 GPa while maintaining a fluid-phase conductivity of ~300 S/m. Bethkenhagen et al. (2017) conducted quantum molecular dynamics simulations of H_2O-NH_3-CH_4 (3:1:1) mixtures at Uranus interior conditions (200 GPa, 5000 K), predicting thermodynamic un-mixing into distinct oxygen-rich (~10 S/m) and hydrogen-rich (~1000 S/m) fluid layers.

This experimental evidence collectively suggests that Uranus's deep interior likely contains a layer where conductive ionic fluids coexist with diamond precipitation. There is a lack of compositional and chemical understanding of the shallow interior of Uranus and Neptune, that our study aims to address.

Previous high-pressure experiments have established a range of conditions under which diamonds can form from carbon-bearing materials. Benedetti et al. (1999) reported diamond formation from methane at pressures above 50 GPa and temperatures exceeding 3,000 K. Hirai et al. (2009) observed diamond formation from CH_4 at pressures above 20 GPa and temperatures near 2,000 K. Although the pressure thresholds are widely accepted, the variation in reported temperatures reflects differences in starting chemistry. Methane requires higher thermal energy to dissociate, whereas mixed systems containing CO_2 may more readily facilitate carbon clustering due to partial oxidation pathways (Akaishi et al., 2000).

For differences in the complex changes occurring within the Diamond Anvil Cells. Kadobayashi et al. (2021) demonstrated that diamond could form from C–H–O mixtures at pressures above 20 GPa and temperatures as low as 1,600 K. They attributed the lowered temperature formation threshold to the catalytic role of oxygen in promoting carbon bonding and destabilizing molecular precursors.

The stability of diamond under planetary conditions can depend on the mixture's chemistry, with oxygen lowering the threshold for its formation. Although shock experiments

and DFT-MD simulations have yielded constraints on diamond formation in hydrocarbon systems at similar conditions (Nellis et al., 1997; Chau et al., 2011), they are limited by the short period of compression. As a result, the long-term behavior of carbon-poor mixtures at more moderate pressures remains largely unexplored. Our approach extends this understanding by applying static compression up to 55 GPa with in situ double-sided laser heating, providing direct access to the phase relations present in the shallow regions of Uranus and Neptune's interiors, where diamond precipitation has been proposed to form and influence planetary structure.

Using laser-heated diamond anvil cell (LHDAC) experiments, we examine the pressure-temperature thresholds for diamond formation across a range of compositions. We look at how oxygen-rich environments, stemming from components like water and isopropanol, combined with ammonia, influence the conditions required for diamond formation. The experimental results presented here aim to offer information for improving models of ice giant interior dynamics, including the role of diamond sedimentation in Neptune's excess heat emission and the debated mantle stratification in Uranus (Helled, 2020). Overall, this work extends our understanding of the composition, phase behavior and thermal evolution of planetary ices, and provides essential constraints on the processes governing diamond formation within ice giant mantles.

4.2 Methodology

A mixture of Synthetic Uranus following the instructions of Nellis (1987). The mixture consisted of water (H_2O, 2.854 ± 0.03 g), ammonium hydroxide with 29% ammonia (NH_4OH, *Alfa Aeasar*, 3.348 ± 0.015 g), and isopropanol (C_3H_8O, *Alfa Aeasar,* 3.798 ± 0.02 g). For each set of experiments a new batch of Synthetic Uranus was made, with the goal of minimizing any loss of isopropanol or ammonia due to their volatility. Table 4.1 lists each mixture's composition, compared to the original composition of Synthetic Uranus, defined by Nellis (1987). Each mixture was then loaded into a Diamond Anvil Cell (DAC). Culet sizes ranged from 200 μm to 500 μm. The sample chamber was drilled to be approximately 1/3 the size of the culet (70 μm – 170 μm). Each sample was then pre-compressed to a pressure in the range from 1 to 5 GPa. Pressure was determined by ruby fluorescence and x-ray diffraction peaks of a metal foil (Pt, Au) placed in the sample chamber. The metal was also used as a laser heating conduit.

Table 4.2. Amounts of each component of Synthetic Uranus (water, ammonium hydroxide, and isopropanol) present for each iteration of Synthetic Uranus in the present study. Below this, I present the molar ratios for the CHNO components of each mixture. The first column is the composition detailed by Nellis et. al. (1988), for a total of 10 g per sample. * SUNW is my Synthetic Uranus mixture, where I left out the amount of water normally needed, to observe what additional phases formed without Ice VII overwhelming the XRD patterns.

	SYNTHETIC URANUS	**SU-1**	**SU-2**	**SU-3**	**SUNW***	**SU-4**	**SU-5**	**SU-6**
	Components							
H_2O	2.854 g	2.842	2.843	2.854	0	2.87	2.856	2.832
C_3H_8O	3.797 g	3.800	3.800	3.819	3.864	3.798	3.795	3.783
NH_4OH	3.348 g	3.356	3.357	3.348	3.347	3.345	3.39	3.336
	Molar Ratios							
C	0.102	0.09	0.09	0.09	0.121	0.09	0.091	0.09
H	0.677	0.678	0.678	0.678	0.682	0.678	0.678	0.678
N	0.031	0.035	0.035	0.035	0.009	0.035	0.035	0.035
O	0.191	0.196	0.196	0.196	0.149	0.196	0.196	0.196

Experiments were conducted at Argonne National Lab's APS HPCAT 16-IDB and Lawrence Berkeley National Lab – Advanced Light Source (LBNL - ALS) 12.2.2 Beamline. The energy for each experiment: $\lambda = 0.4945 - 0.5391$ Å. X-Ray diffraction data was taken in situ for each experiment and upon compression and decompression. Laser heating occurred at both locations using spectroradiometry to determine temperature, implementing a modified peak scaling method to measure temperature in the laser-heated diamond anvil cell (Kunz et. al., 2018). Raman Spectroscopy was used for room-temperature vibrational measurements with a 532 nm laser on a Horiba LabRAM HR Raman Spectrometer at UC Santa Cruz in Dr. Quentin William's lab.

4.3 Results and Discussion

4.3.1 Room Temperature Compression

Room-temperature compression of Synthetic Uranus mixture revealed a phase separation between an ammonia-dominated solid and crystalline water ice (Ice VII). To identify the ammonia-bearing phase we first compressed pure ammonium hydroxide under identical conditions to Synthetic Uranus. Upon reaching 4 GPa, the sample crystallized into ammonia hemi-hydrate II (AHH-II), coexisting with Ice VII. Figure 4.1 illustrates the characteristic diffraction peaks corresponding to the AHH-II phase. Peak positions were determined through our custom Igor Pro script and its equation of state. The observed diffraction peaks were indexed by comparison to published AHH-II patterns from Ma et al. (2012) and Andriambariarijaona et al. (2023). Specifically, our measured *d*-spacings for AHH-II corresponded to the equation of state presented in these works.

Our X-ray diffraction (XRD) analysis also identifies Ice VII. This is the dominant phase within the sampled pressure-temperature conditions, comprising approximately 70% of the

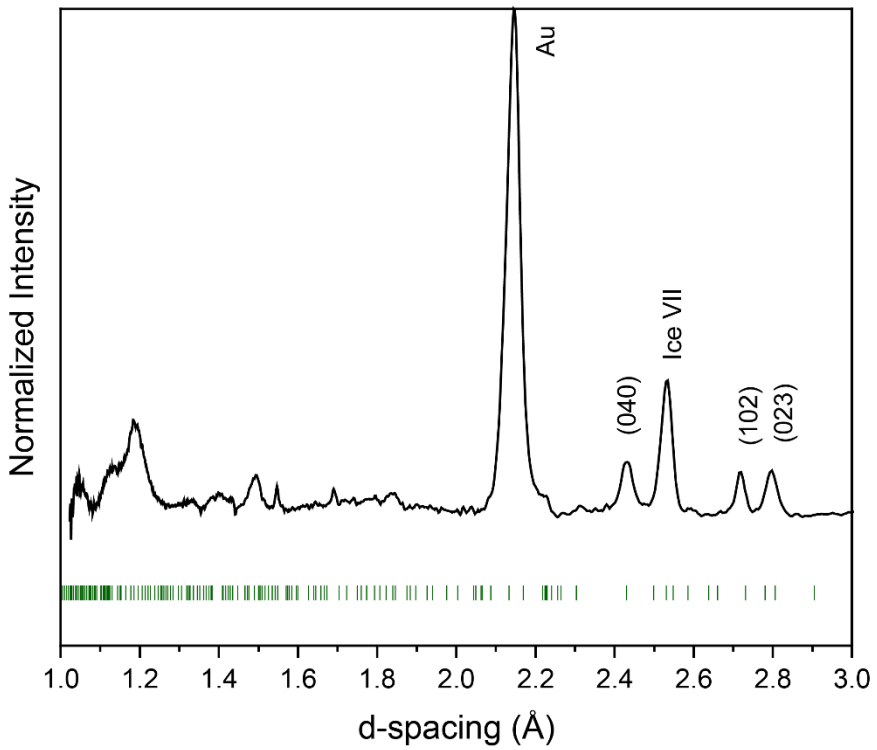

Figure 4.1. X-Ray Diffraction pattern of Synthetic Uranus depicting the 3 identifying peaks of Ammonia hemi-hydrate-II ((040), (102), and (023)). This was a mixture of Synthetic Uranus where only ammonium hydroxide and isopropyl alcohol were present, negating the overwhelming presence of Ice VII. Visually, there was a phase separation from Ice VII within the cell. These were identifiable in comparison to Wilson et. al. (2015).

simulated mantle volume. This conclusion is based on characteristic diffraction peaks matching known Ice VII patterns. This approach provides robust semi-quantitative volume fractions, but uncertainties remain due to potential peak overlaps with other phases, effects of texturing, and limitations in signal-to-noise ratio. Nonetheless, the overwhelming intensity of the Ice VII peaks relative to others supports its dominance. The stability of Ice VII under the present experimental conditions aligns with previous work indicating its persistence above pressures of ~4 GPa (Antsyshkin et al., 2010) and reinforcing its expected prevalence in ice giant mantles.

The predominance of Ice VII suggests it plays a crucial role in governing the early-stage rheology of ice giant mantles due to its high viscosity and mechanical stability. Thermal evolution models (e.g., Redmer et. al., 2011) propose that such viscous layers can form stagnant, conductive boundary regions that inhibit convective heat transport. This hypothesis is consistent with Voyager II observations of Uranus' notably low intrinsic heat flux (< 0.1 W/m^2; Pearl et al., 1990), which can be explained by a high-viscosity Ice VII-dominated layer overlying more mobile phases, such as superionic water or a fluid ocean (Millot et al., 2019). The suppressed convection reduces advective heat transfer, trapping heat in the interior and leading to Uranus's anomalously low thermal emission relative to Neptune (Podolak et al., 2019).

However, uncertainties remain regarding the long-term stability of this stratification. Diamond formation, a likely decomposition product, could further modify the dynamics and stability of these layers. During compression of Synthetic Uranus (containing water, ammonium hydroxide, and isopropanol), the high-water content resulted in high-intensity Ice VII diffraction peaks that obscured weaker reflections from the ammonia-bearing phase. To mitigate this, we prepared a second mixture excluding the bulk water content, consisting only of ammonium hydroxide and isopropanol in the ratios presented for Synthetic Uranus (Table 4.1).

This mixture was loaded into a diamond anvil cell with a rhenium gasket pre-indented to ~30 μm thickness and drilled to have a ~120 μm diameter sample chamber. Compression was carried out incrementally in 1–2 GPa steps to a maximum pressure of 10 GPa, confirmed via ruby fluorescence. After each pressure step, the sample was equilibrated for at least 30 minutes before XRD collection to ensure phase stability. Under these conditions, Ice VII remained the dominant phase, but the reduced water fraction allowed consistent identification of AHH-II reflections.

The disordered molecular alloy (DMA) phase of ammonia hemi-hydrate was not identifiable in our XRD patterns. The DMA phase typically forms above 25 GPa (Robinson et. al., 2017), and our room temperature ammonium hydroxide experiments remained below this pressure threshold.

Although isopropyl alcohol was not directly visible in any XRD patterns, Raman spectroscopy confirmed its continued presence through its carbon-hydrogen vibrational modes Specifically, while the characteristic ammonium ion (NH_4^+) peak disappeared by 4 GPa, the C–H stretching vibrational modes (~3000 cm^{-1}) associated with isopropyl alcohol persisted during compression. This indicates that upon compression, while not observed in our XRD patterns, C-H bonding remains through room-temperature compression.

4.3.2 Laser Heating and Diamond Formation

Benedetti et al. (1999) conducted laser-heated diamond anvil cell (LHDAC) experiments on methane from 10 to 50 GPa and between 2,000 and 3,000 K. Their work demonstrated that methane first dissociated into heavier hydrocarbon chains (e.g., ethane) and hydrogen before

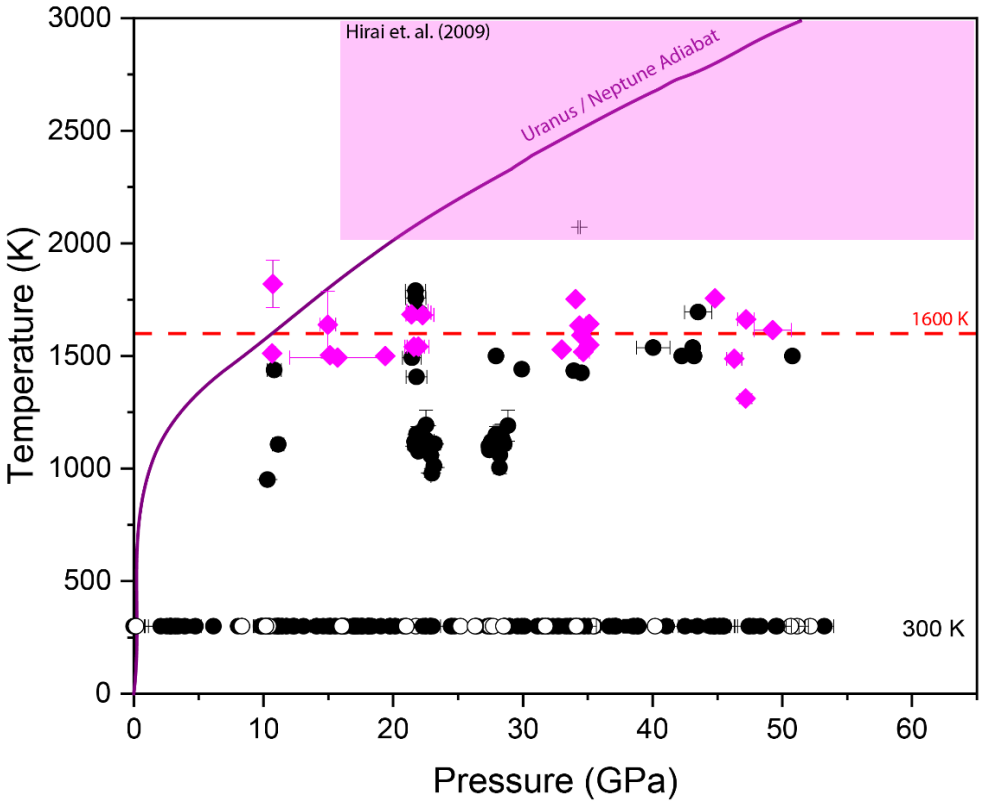

Figure 4.2 Pressure and Temperature plot showing the conditions at which the present work was conducted. The shaded pink box is the range of conditions that Hirai et. al. (2009) found for diamond formation. The dashed red line is the temperature limit that Kadobayashi et. al. (2021) proposed for diamond formation in C-H-O mixtures. The presence of oxygen lowers the temperature needed to form diamond. Filled (●) circles are points taken while compressing and heating the material. Open circles are points taken upon decompression at 300K. Magenta data points are where diamond formation was seen during laser heating. The remaining points are pressure-temperature conditions where XRD measurements were taken. The Adiabat is taken from Guillot et al. (2015).

transitioning to diamond, with temperature playing a more dominant role over pressure in driving the reaction kinetics. However, their study did not identify a sharp pressure-temperature boundary; instead, they found that diamond yield increases gradually with temperature.

Hirai et al. (2009) expanded on these findings by mapping methane's phase transitions in the C–H system from 10 to 81 GPa. They identified four distinct temperature regimes: below 1,100 K, solid methane retained its molecular structure; at 1,100–2,200 K, melting and ethane formation occurred; at 2,200–3,000 K, long-chain hydrocarbons polymerized; and above 3,000 K, diamond formed. Both studies focused on methane systems, leaving open the question of how planetary ice mixtures, such as those containing water or ammonia, might alter these thresholds.

Kadobayashi et al. (2021) showed that methane-water (C–O–H) systems lower the temperature of formation to ~1,600 K, and our Synthetic Uranus experiments show that icy mixtures, with ammonia present, can further reduce the temperature barriers, with diamond forming at 1,500 K across a broad pressure range.

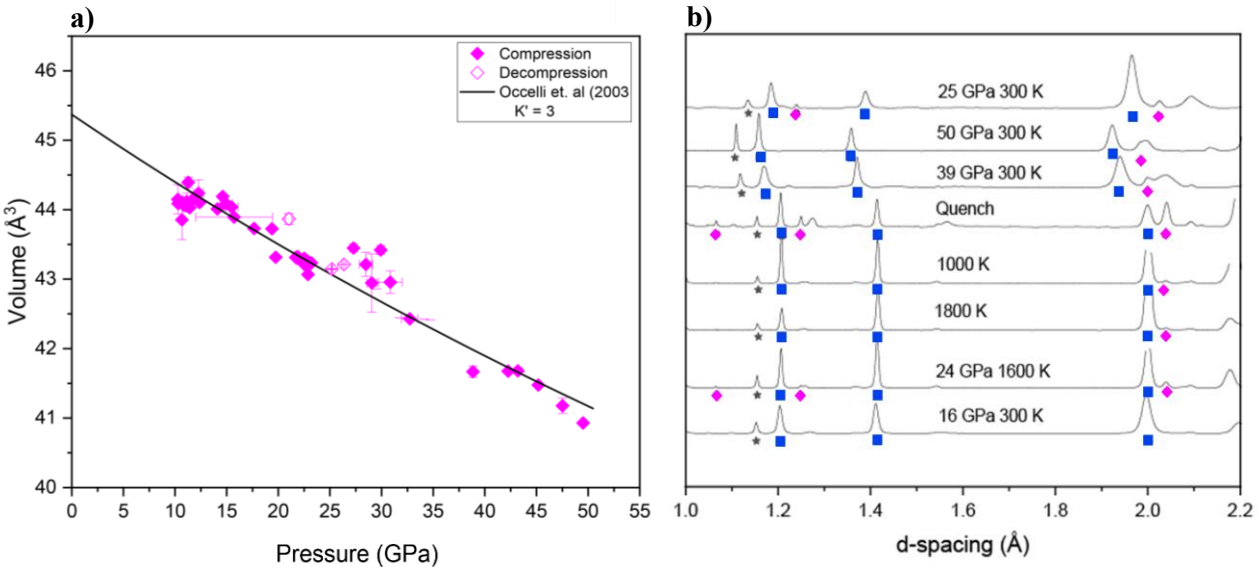

Figure 4.3. (a) A volume versus pressure plot for diamond formed in the present study compared with the equation of state of Occelli et. al. (2003) (K_0 = 444 GPa and K_0' = 3). The open data points were taken upon decompression. (b) A stacked XRD pattern plot depicting the progression of the Ice VII (▪), Gold (★), and Diamond (♦) peaks through compression, laser heating, and decompression. Diamond began forming near 1600 K, consistent with Kadobayashi et. al.'s (2021) proposed threshold.

To validate our identification of diamond, we compared our diamond volume-pressure data with the established equation of state (EOS) from Occelli et al. (2003), as illustrated in Figure 4.3. The X-ray diffraction patterns collected during compression and decompression show the characteristic diamond peaks, with the (111) reflection serving as the primary indicator of diamond formation. In many cases, the secondary (220) peak was also detected, reinforcing the identification of diamond. In situ X-ray diffraction measurements, combined with post-experiment Rietveld refinement, allowed us to calculate the pressure and temperature conditions at which diamond formation occurred during laser heating. Upon decompression at room temperature, diamond persists in the sample chamber, in accord with the well-known metastability of diamond at 300 K. Our results indicate that the remaining fluid phase undergoes significant compositional change due to the extraction of carbon into the diamond phase.

I present additional data (Figure 4.4) which agrees well with Occelli et. al.'s (2003) results. The inset within this plot is an example of our XRD pattern at 25 GPa and the main (111) and (220) peaks present. Due to challenges in sample recovery, we were unable to perform a detailed chemical analysis of the residual liquid, leaving its exact composition unresolved. Future experiments, with improved recovery techniques, could provide further insight into the phases.

Kadobayashi et al. (2021) showed a clear sequence: methane hydrate decomposition near 600 K, formation of hydrocarbons around 1200 K, and diamond formation at approximately 1600 K and pressures between 13 and 45 GPa. They proposed that water, particularly the presence of oxygen, acts as a catalytic medium, lowering the temperature needed for carbon bond rearrangement and diamond formation.

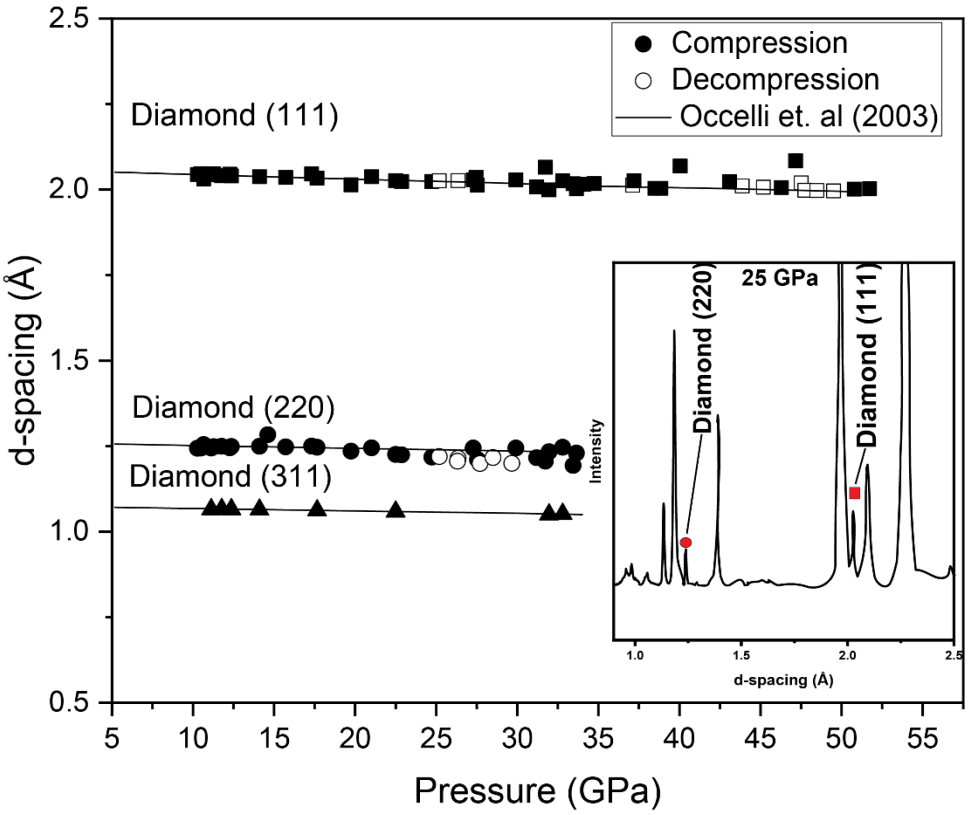

Figure 4.4. Diamond d-spacing shift with pressure from our XRD patterns. The (111) peak is the main identifier of diamond being present within the sample. The (220) peak is visible on most patterns, but not all. Additionally, the (311) peak was difficult to identify in most patterns. (▪) indicates the (111) peak, (●) indicates the (220) peak, and (▲) indicates the (311) peak. The **inset** is a XRD pattern at 25 GPa, post heating, depicting the diamond peaks present.

Our Synthetic Uranus experiments build upon and extend these results by examining more complex mixtures that include ammonia, conducted at pressures reaching up to 55 GPa. Despite varying pressures, diamond formation in our system occurs at temperatures as low as 1500 K, suggesting that the presence of ammonia further decreases the temperature required for diamond formation.

Our findings challenges the present model that diamond formation is confined to the deep, high -pressure interiors of ice giants, implying instead that diamond formation initiates at shallower mantle depths. Such early-stage diamond formation has consequences for models of planetary carbon cycling, stratification, and thermal evolution of ice giants. For example, diamond rain could contribute to Uranus's internal heat flux through gravitational settling and frictional heating (Lobanov et al., 2013). Moreover, precipitation of diamonds may influence convective motions in conductive ice layers, offering a mechanism to help explain Uranus's unusual magnetic field (He et. al., 2022).

The contrast between the present Synthetic Uranus results and past studies underscores a key insight: while methane purity dictates reaction kinetics in simplified systems, planetary relevance requires the study of multi-phase, multi-component analogs. In Synthetic Uranus, diamond formation occurs at ~1,500 K, a temperature notably lower than in Benedetti's methane-only experiments (2,000–3,000 K) and distinct from Kadobayashi's tertiary C–O–H system (~1,600 K). This supports the hypothesis that Uranus and Neptune's mantles may host diamond-forming regions, or "diamond hail."

In our experiments, the diamond formed has the same kinetic stability as diamond formed through other methods and remains stable on decompression to zero pressure. In contrast, Ice VII persisted throughout compression and decompression, but only at pressures above the known phase transition to Ice VI at 4 GPa. This behavior implies that while ice phases follow reversible transitions, diamond exhibits metastability: diamonds formed at high pressure can persist at lower pressures during planetary cooling and ascent.

Using the 10% carbon concentration measured in our Synthetic Uranus mixtures and assuming a mantle mass on the order of 3.5×10^{26} kg, we estimate the gravitational potential energy released by diamond sedimentation as follows: considering diamonds settling through a mantle thickness of approximately 10^7 meters under gravity of ~10 m/s², and accounting for the density contrast between diamond (~3500 kg/m³) and mantle ices (~1500 kg/m³) (all values from Bethkenhagen et al., 2017), the total energy release could reach ~10^{33} joules. (Calculations presented in Appendix B).

This energy is comparable to, and in some cases exceeds, the total radiogenic heat available in ice giant interiors. It arises from the bulk gravitational settling of a substantial mass of dense material through the mantle, rather than localized chemical reactions or conduction. Even at these lower bounds, this energy constitutes a substantial heat source capable of influencing the thermal evolution, convective dynamics, and magnetic field generation of ice giant planets (Cheng et al., 2023).

In Neptune, continued carbon sedimentation could enhance convective motions by releasing gravitational energy as diamonds descend, contributing to the planet's sustained heat flux (Nettelmann et al., 2013). In contrast, Uranus's low intrinsic luminosity suggests a more stagnant interior, where diamond accumulation may trap heat and suppress energy release. The chemical consequences of carbon sequestration also carry magnetic implications. Sequestering carbon as diamond depletes carbon from the conductive fluids, potentially enhancing the abundance of charge carriers available for dynamo generation (Redmer et al., 2011).

Thus, hydrogen released during diamond formation, either as molecular H_2 or ionic species, may enhance fluid conductivity, especially in Neptune's convective dynamo shell (Helled et al., 2020; Nellis et al., 1997). Extrapolating to exoplanets, our demonstration of diamond formation up to at least ~50 GPa supports models suggesting that carbon-rich super-Earths, such as 55 Cancri e, may undergo similar differentiation, forming deep diamond layers that affect their thermal and magnetic evolution (Madhusudhan et al., 2012).

4.4 Conclusion

The chemical impact of our findings is significant because Synthetic Uranus contains only 10% carbon by mass, creating new opportunities to investigate how limited-carbon reservoirs can yield diamond formation under extreme conditions.

For comparison, Cheng et al. (2023) conducted ab initio molecular dynamics simulations to predict the stability of carbon phases within C–H–O mixtures at Uranus-relevant pressures and temperatures. Their results indicated that at least ~15% carbon would be necessary for diamond formation to become thermodynamically favorable throughout the mantle. Their approach is combining first-principles free energy calculations with extensive sampling of phase equilibria. In contrast, our experiments show that even with 10% carbon, below Cheng et al.'s (2023) threshold, diamond can precipitate under similar pressure-temperature conditions. Kinetic factors or compositional effects may further lower the formation temperature in real planetary mixtures. Our observation that ammonia reduces the onset temperature for diamond formation by approximately 100 K highlights a possible catalytic role for nitrogen-bearing volatiles in facilitating diamond formation.

By focusing exclusively on static compression over intermediate pressures and temperatures (10–50 GPa, 1,000–2,000 K), our work offers an experimental framework relevant to the upper mantles of Uranus and Neptune. Central to this study is the stratification of diamond within volatile-rich, icy mantles, where carbon precipitation may influence heat transport, buoyancy, and mantle convection. Although previous theoretical and experimental work indicates diamond formation can strongly affect ice giant thermal evolution (Nettelmann et al., 2013; Redmer et al., 2011), the spatial distribution and kinetics of diamond within those mantles remain poorly constrained. Our observations of diamond formation and its persistence during decompression provide direct evidence that diamond can form and remain stable under planetary-relevant conditions, thereby strengthening the link between laboratory experiments and models of ice giant interior dynamics.

Future work should examine Synthetic Uranus below 10 GPa, while remaining at similar temperatures, to address the issue of sample recovery after decompression, and find methods of further identifying structures of the diamond formed.

Chapter 5

Carbon-Poor Synthetic Planetary Ices at High Temperature and Pressure

5.1 Introduction

Unlike Earth's interior, ice giants are hypothesized to lack a well-defined core-mantle boundary, instead, hosting a gradual transition from molecular to dissociated fluid states where carbon undergoes complex phase transitions (Helled & Fortney, 2020). The behavior of carbon at low concentrations (≤10% by molar fraction) in these environments remains unknown, as diamond precipitation could drive large-scale material stratification, influence thermal conductivity, and modulate convective processes responsible for magnetic field generation (Vazan et al., 2018; Scheibe et al., 2021).

The geodynamic implications of diamond sedimentation in ice giants is influenced by compositional gradients, thermal gradients, diamond grain size, and the heat released during sinking. Vazan et al. (2018) modeled the thermal evolution of Uranus by incorporating "diamond hail." They found that micron-sized grains enhanced radiative cooling. However, these models assume a homogeneous carbon distribution throughout the mantle, neglecting the heterogeneous phase separation observed in experiments (Bethkenhagen et al., 2017). The gravitational energy released during diamond sedimentation can delay planetary cooling and contraction, influence mantle convection patterns, and potentially create compositional stratification, all of which impact the long-term thermal and structural evolution of these planets.

Recent laser-heated Diamond Anvil Cell (LHDAC) studies by Scheibe et al. (2021) on H_2O–CH_4–NH_3 mixtures (20–60 GPa, 2500–4000 K) revealed that carbon-rich droplets form diamond at ~45 GPa, while nitrogen-rich regions preferentially form carbides. This microstructural heterogeneity suggests that diamond precipitation may not occur uniformly throughout the convecting mantle.

Despite these advances, no studies have explored diamond formation in carbon-poor (< 10% C) C-H-N-O ices across the pressure-temperature range relevant to shallow ice giant mantles (0–40 GPa, 1400–2000 K). The outermost mantle regions represent the initial chemical environment where carbon's fate is either to remain within hydrocarbons, form diamond, or polymerize into refractory organics. The influence of oxygen and nitrogen content on the thermodynamic stability field of diamond in these dilute systems remains unexplored experimentally.

To address this gap, we conducted laser-heated Diamond Anvil Cell (LHDAC) experiments on synthetic ices with systematically varying C-H-N-O ratios. This chapter details these experiments on carbon-poor Synthetic Uranus mixtures, exploring how varying concentrations of carbon, nitrogen, and oxygen affect the pressure-temperature parameters for diamond formation. We present results from eight distinct C-H-N-O mixtures (Table 5.1), using synchrotron-based laser-heating and X-ray diffraction combined with Raman spectroscopy to map the formation of diamond against competing phases. These findings provide new experimental constraints for multi-component ices, exploring the pressure, compositional, and temperature requirements for diamond formation in regimes directly relevant to the outer mantles of ice giant planets.

5.2 Methodology

I made eight mixtures with varying concentrations of carbon, oxygen, nitrogen and hydrogen, adjusting the specified concentrations of Nellis' (1988) Synthetic Uranus. The mixtures consisted of water (H_2O, 2.854 ± 0.03 g), ammonium hydroxide with 29% ammonia (NH_4OH, *Alfa Aeasar*), and isopropanol (C_3H_8O, *Alfa Aeasar*). For each set of experiments a new batch of each mixture was made to minimize any loss of isopropanol or ammonia due to their volatility.

Table 5.1 depicts each mixture of C-H-N-O molar ratios compared to the original Synthetic Uranus mixture derived by Nellis. Within the table, columns A, B, and C are mixtures where we only adjusted the amount of isopropanol to change our carbon concentration. Columns D, E, and F are our "oxygen rich" mixtures. Water and isopropanol were varied to achieve a higher concentration of oxygen relative to Synthetic Uranus and the lower concentration of carbon. For the samples in the last two columns, G and H, the amounts of ammonium hydroxide and isopropanol were varied to achieve low carbon content and a higher nitrogen content compared to Synthetic Uranus.

Each mixture was then loaded into a diamond anvil cell (DAC). Culet sizes ranged from 200 μm to 500 μm. The sample chamber was drilled to be approximately 1/3 the size of the culet (70 μm – 170 μm). Each sample was then pre-compressed to range from 1 to 5 GPa. Pressure was determined by the x-ray diffraction peaks of a metal foil (Pt, Au) placed in the sample chamber. This metal was also used as a laser heating coupler.

Table 5.1. Molar ratios of each of the eight carbon-poor mixtures. Synthetic Uranus denotes the mixture defined by Nellis et. al. 1988. Columns CPA, CPB and CPC are our "carbon adjusted" samples, with the amount of isopropanol adjusted to change the carbon abundance. Columns ORD, ORE, and ORF are our "oxygen rich" samples, where the oxygen abundance is larger than Synthetic Uranus. Columns NRG and NRH are our "nitrogen rich" samples where the ammonium hydroxide was adjusted to increase the nitrogen abundance compared to Synthetic Uranus.

	Synthetic Uranus	**CPA**	**CPB**	**CPC**	**ORD**	**ORE**	**ORF**	**NRG**	**NRH**
C	0.102	0.087	0.066	0.038	0.038	0.052	0.039	0.093	0.020
H	0.677	0.678	0.679	0.681	0.681	0.668	0.667	0.684	0.695
N	0.031	0.033	0.038	0.038	0.038	0.005	0.002	0.050	0.084
O	0.191	0.202	0.217	0.237	0.241	0.275	0.291	0.173	0.201

Experiments were conducted at the Lawrence Berkeley National Lab – Advanced Light Source (LBNL-ALS) 12.2.2 Beamline. The energy for each experiment ranged from 23 to 30 keV. In situ X-Ray diffraction data were collected upon compression and decompression, with double-sided laser heating. During laser heating, temperature is determined through spectroradiometry (Kunz et. al. (2018)). Additionally, Raman spectroscopy was used for post-heating identification of diamond. Raman was collected at the Department of Earth and Planetary Sciences at the University of California, Berkeley in Dr. Penny Weiser's Lab. The system used was a WiTec Alpha 300R Raman spectrometer. A green (532 nm) solid laser was used and laser focused as an excitation source with a 20x objective (Leticia). The system is a TruePower system which allows for in-fiber power adjustments of <0.1 mW.

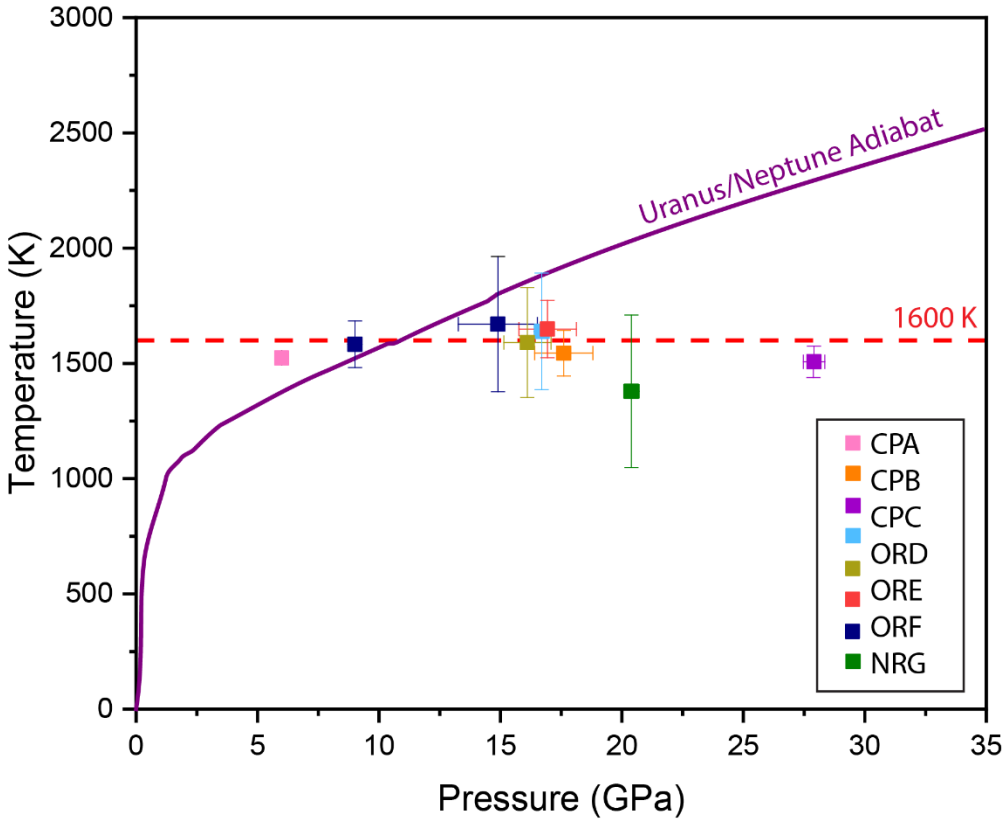

Figure 5.1. Each of the eight samples within pressure – temperature space. While there are many XRD patterns with diamond present, it was difficult to identify as the sample was heating. Each point was taken during heating, and showed diamond was present. The dashed line at 1600 K is Kadobayashi et al.'s (2021) threshold for diamond formation. The Uranus/Neptune Adiabat was taken from Guillot et al. (2015).

5.3 Results and Discussion

Diamond formed across all eight compositions: "carbon-poor" (CPA, CPB, CPC), "oxygen-rich" (ORD, ORE, ORF), and "nitrogen-rich" (NRG, NRH). Each system contains <10% carbon and was stable through pressures of 10–50 GPa and temperatures of 1400–2000 K, as shown in Figure 5.1. Diamond formation was then confirmed by both *in-situ* X-ray diffraction and post-laser heating X-ray diffraction.

This is shown by the consistent emergence of the diamond (111) and (220) peaks. Identification of peaks was determined through the equation of state of diamond from Occelli et al. (2003). Raman spectroscopy confirmed the formation of diamond through the shift of its highest frequency peak (Boppart et al., 1985), shown in Figure 5.2. Our data confirm that diamond forms in these compositional and pressure-temperature conditions, with the reduced abundance of carbon (increased oxygen and nitrogen abundances) apparently not affecting diamond-formation pressures or temperatures.

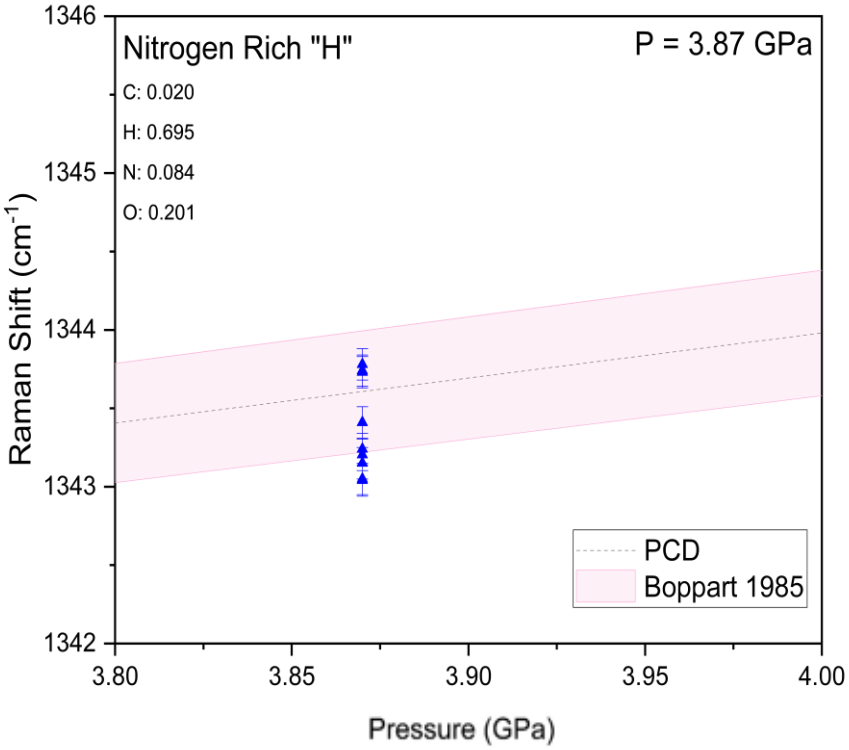

Figure 5.2. Polycrystalline Diamond (PCD) Raman peak frequency following decompression to 3.87 GPa at room-temperature. Each point represents the measured Raman shift of the strongest frequency diamond peak at different positions around the sample chamber. The dashed line is a reference from Boppart (1985), and the shaded band indicates the reported error range.

Diamond sequestration can alter mantle dynamics. The coexistence of diamonds with Ice VII in our high-pressure mixture forms a heterogeneous solid mixture with varying solid concentrations throughout. Fortney and Nettelmann (2010) argued that such gradients can inhibit large-scale convection by stabilizing density layering; in Uranus, where the observed heat flow is anomalously low, this stratification could suppress adiabatic upwelling and limit cooling efficiency. Diamond formation effectively removes carbon from the convective fluid, creating feedback. Then as carbon depletes in the upper mantle, convection further weakens, trapping heat in the deep interior.

Our observation that diamond formation occurs within diverse local compositions (e.g., oxygen-rich and nitrogen-rich domains, like our oxygen rich and nitrogen rich mixtures) implies that spatial heterogeneity in diamond precipitation can arise throughout the mantle, amplifying its dynamical impact. This clarifies that “heterogeneous” here refers to spatial variability in the locations of diamond formation, as distinct from the non-homogeneous phase separation described above. Additionally, our data enable estimation of the gravitational energy budget associated with diamond sedimentation.

For Uranus, the gravitational potential energy released by diamond settling could reach 10^{33} J (Appendix B.2), which is comparable to the planet's missing thermal energy (Helled and Stevenson, 2017). This estimate assumes that ~5% of the mantle mass (~0.5 Earth masses) consists of carbon that forms diamonds descending through a mid-mantle distance of ~10^7 m.

While our experiments do not directly measure density contrasts, theoretical models predict sufficient differences in density, 3.5 g/cm³ for diamond compared to 1.5–1.8 g/cm³ for high-pressure ices (Bethkenhagen et al., 2017), to enable efficient sedimentation. Finally, our observed spatial variability in diamond distribution suggests that localized sedimentation plumes may contribute to Uranus's asymmetric luminosity, with diamond-rich downwelling releasing gravitational energy intermittently rather than through uniform rain. This is consistent with thermal evolution models indicating that Uranus's luminosity is influenced by compositional gradients and transient convective erosion of insulating layers, leading to spatially and temporally variable energy flux to the outer envelope (Scheibe et al. (2021).

Our ORD – ORF samples (O:C ratios up to 8:1) formed diamond as readily as the other carbon-poor mixtures. This contrasts with oxidized systems such as CO_2-rich ices, where high-pressure studies have observed carbonate formation stabilized over diamond at comparable pressures (e.g., Ghosh et al., 2017). Our experimental conditions favor diamond as the terminal carbon phase. Similarly, although theoretical predictions suggest that nitrogen incorporation

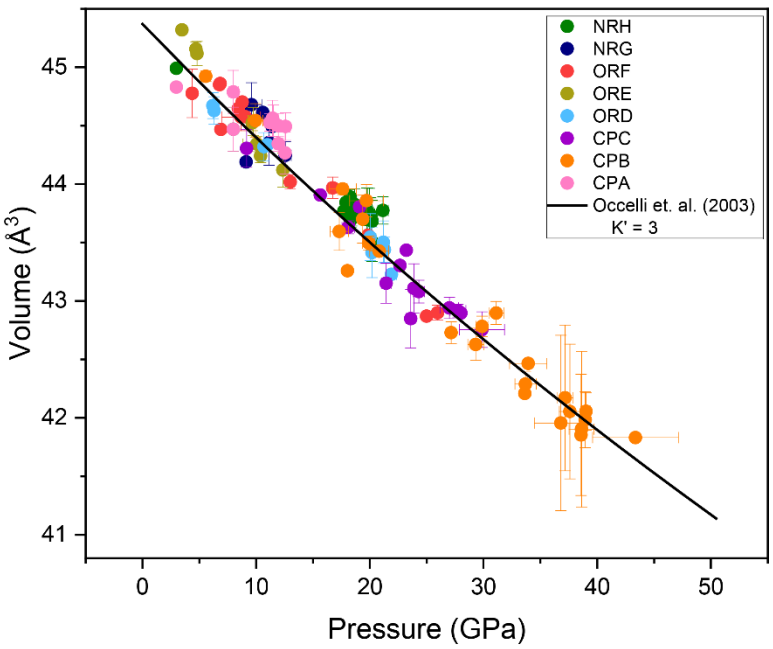

Figure 5.3. Pressure - Volume plot for each experiment that had diamond present in its XRD patterns. Each color depicts a different mixture (Table 3.1). Data are compared to Occelli et. al's (2003) equation of state (K_0 = 444 GPa and K' = 3). Error bars are presented for all data; if not seen, then the error exists within the size of our data point.

might stabilize polymeric carbons or carbon nitrides (Tschauner et al., 2018), our NRG–NRH samples consistently exhibited unaltered diamond formation below 50 GPa.

The pressure-volume plot (Figure. 5.3) summarizes diamond-bearing experiments through our measurements of diamond's compression behavior in carbon-poor carbon-hydrogen-nitrogen-oxygen systems. No matter the carbon content, our results agree with the equation of state for diamond (Occelli et. al., 2003). The increased uncertainty in the data with increasing pressure is due to peak overlap of the diamond (111) peak with the (100) peak of Ice VII.

Our demonstration of diamond formation at just 2% carbon (Figs. 5.1, 5.3–5.4) extends "diamond hail" models to cooler exoplanetary systems. Interior models (Valencia et al., 2007; Howe et al., 2014) show that the 20 GPa conditions of our observed formation threshold occur at approximately 0.3 planetary radii in 5 $M_{\oplus}$ mini-Neptunes, depths easily reached even with 1000 K isotherms. This implies that carbon sequestration could operate in modestly heated exoplanets, with heating due to sedimentation (~10^{27} J for 2 $M_{\oplus}$ mantles; Baraffe et al., 2008) potentially delaying planetary contraction. Our results using chemically complex CHNO mixtures better replicate the compositions of planetary mantles than do previous experiments, suggesting that diamond formation and carbon cycling in planetary interiors may be more efficient than predicted by current models.

Our experiments with laser heating lasting seconds to tens of seconds, produced clear diamond formation across all compositions, The presence of AHH-II in our XRD patterns confirms that diamond formed preferentially over more polymerized carbon phases, or carbon chains, under these conditions. This preference aligns with Bastea et al. (2017), who concluded that rapid heating and compression under extreme, short-timescale conditions facilitate nanodiamond formation by lowering formation conditions when compared to equilibrium predictions. Our observation of diamond formation from <10% carbon concentration without requiring extreme compression suggests that such thresholds may be more readily achieved in planetary interiors than previously modeled.

This work shows diamond formation as a robust process in carbon-poor (<10% C) planetary ices across 10–50 GPa and 1400–2000 K, with implications for ice giant structure and evolution. The consistent emergence of diamond (111) XRD peaks (Figure. 5.1) across all compositions, despite varying oxygen and nitrogen ratios, demonstrates that carbon concentration and pressure-temperature conditions are the primary drivers of formation. This challenges hypotheses like Kadobayashi et al.'s (2021) oxygen catalysis model, which predicted shifted thresholds. Our Raman data (Figure. 5.2) further supports this: peak positions align with diamond (Boppart et al., 1985), with no systematic shift due to oxygen and nitrogen abundance variations.

5.4 Conclusion

Our experiments show that diamond forms across all tested compositions (2-10% C) at pressures as low as 5 GPa and temperatures of 1500 K (Figure. 5.1), with formation thresholds showing no dependence on oxygen or nitrogen content (Figure. 5.3). The consistent appearance of diamond (111) X-ray diffraction peaks suggests carbon conversion proceeds even in these carbon-poor systems. In planetary contexts, patchy diamond formation could create regional density anomalies in ice giant mantles, potentially contributing to the observed luminosity differences between Uranus and Neptune.

For ice giants, our results indicate that "diamond hail" can initiate at shallower interior depths (~5 GPa, approximately 0.8 Uranus radii) than previously predicted for pure methane systems, where ab initio simulations place diamond formation onset above ~10 GPa (Wilson & Militzer, 2010). The observed insensitivity to composition simplifies interior models by removing the need for complex chemical corrections, implying that local pressure-temperature conditions primarily govern diamond formation. Although our experiments do not directly address sedimentation dynamics, the low pressures needed for diamond formation provide a new constraint for planetary evolution models (e.g., Helled & Stevenson, 2017).

These findings can also extend to exoplanetary systems: water-rich worlds with carbon abundances ≥ 2% may form stable diamond layers at accessible mantle pressures, which can alter their thermal evolution by introducing an additional heat source due to diamond separation: the gravitational energy released during diamond sedimentation can delay planetary cooling and contraction, influence mantle convection patterns, and potentially create compositional stratification, all of which impact the long-term thermal and structural evolution of these planets (Madhusudhan et al., 2012).

Future work is necessary to further investigate formation of diamond in carbon-poor materials, with a larger spread of pressure, temperature, and compositional mixtures, as well as the addition of scanning or transmission electron microscopy (SEM or TEM) to determine diamond grain size, shape, and texture. Electrical conductivity measurements could be used to look for the presence of superionic ice phases.

Chapter 6

Dynamic Compression of Cyclohexane

6.1 Introduction

The study of hydrocarbons under extreme conditions is useful for understanding high-energy-density (HED) physics, planetary interiors, and inertial confinement fusion (ICF) applications. Cyclohexane (C_6H_{12}), a hydrogen-rich ring hydrocarbon, serves as an analog for hydrogen-dominated systems found in many different planets, including Uranus and Neptune.

Under static compression, hydrocarbons exhibit complex behaviors such as polymerization and diamond formation (Benedetti et al., 1999; Kraus et al., 2017), but their dynamic response under shock compression, particularly when pre-compressed, remains less explored. Dynamic loading with pre-compression in diamond anvil cells (DACs) allows access to off-principal Hugoniot states, enabling investigations of phase transitions and metallization at conditions relevant to planetary interiors (Jeanloz et al., 2007; Tabak et al., 2024). We also employed pre-compression because cyclohexane is a liquid at ambient conditions.

The C-H phase diagram (Figure 6.1) reveals a rich landscape of dissociative and metallization transitions at pressures exceeding 100 GPa and temperatures above 5,000 K (Eggert et al. 2010; Kraus et al. 2023). For cyclohexane, shock compression experiments along off-principal Hugoniots can probe whether its behavior aligns with linear-chain hydrocarbons like polyethylene (CH_2) or diverges due to its ring structure.

Prior work on methane (CH_4) and polystyrene (CH) shows non-linearities in shock velocity (U_s) versus particle velocity (U_p) relations, often correlated with dissociation and insulator-to-conductor transitions (ICT) (Tabak et. al. 2024; Barrios et al. 2010). These features are thought to arise from bond breaking and the formation of metallic hydrogen or carbon clusters (Weir et al. 1996; Celliers et al. 2018).

Cyclohexane's Us-Up vs Up relationship (Figure 1.2) exhibits deviations from linearity at particle velocities of 3.8 – 4.8 km/s, suggesting dissociation or phase transition. Unlike linear alkanes, ring hydrocarbons like cyclohexane and benzene (C_6H_6) show pronounced U_s - U_p slope changes, possibly due to changes in their cyclic structures under compression (Ree 1979; Frost et al. 2024).

Pre-compression further modifies these paths, as demonstrated by recent Diamond Anvil Cell experiments on methane, where metallization occurred at lower pressures compared to principal Hugoniot data (Tabak et al. 2024). By extending these methods to cyclohexane, we aim

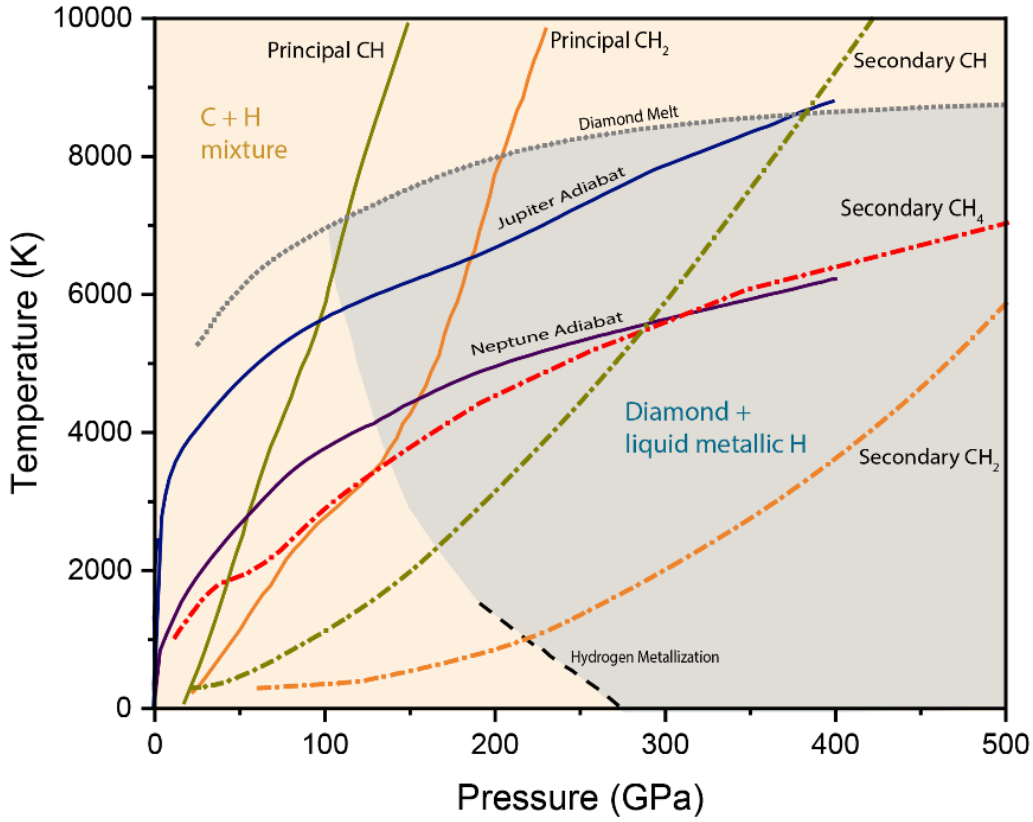

Figure 6.1. Phase diagram of the C-H system showing principal Hugoniots for CH and CH_2 (Barrios et. al. (2010), and Hartley et al., 2018); their second-shock (secondary) Hugoniots from initial densities, 2 g/cc are shown (LANL Hugoniot Data, 1999, SESAME 7592, 7171) which bracket our planned experimental P-T paths at 100 – 400 GPa and >5000 K. Second-shock (secondary) Hugoniot for CH_4 (~0.5 g/cc (Sherman et al., 2012) is shown for comparison, as are adiabatic profiles for temperatures inside Jupiter and Neptune. Darker tan region indicates where diamond formation and hydrogen metallization have been observed under dynamic loading (Weir et al., 1996, Kraus et al., 2023, Kraus et al., 2017). Diamond melt line is also indicated (Eggert et al., 2010).

to resolve whether its dissociation thresholds and reflectivity trends align with theoretical predictions for hydrogen-rich systems (Sesame tables 7592, 7171; Sherman et al. 2012).

Optical diagnostics, including velocity Interferometer for Any Reflector (VISAR) and streaked optical pyrometry (SOP), provide insights into these transitions. Reflectivity

measurements, for instance, can signal the onset of metallization, as observed in shock-compressed hydrogen (Celliers et al. 2018) and methane (Brygoo et al. 2015, Tabak et. al. 2024). In cyclohexane, a rise in reflectivity above 150 GPa (Figure 6.3) may indicate the formation of a conductive fluid phase, while U_s-U_p discontinuities could mark carbon-carbon bond breaking (Kraus et al. 2017).

The implications of the present work extend to planetary science and ICF. In ice giants, dissociation and metallization of hydrogen and hydrocarbons likely influence thermal transport and magnetic field generation (Soyuer et al. 2020; Nettelmann et al. 2013). For ICF, understanding equation of state (EOS) non-linearities in ablator materials like CH and CH_2 is essential for optimizing capsule stability (Orth et. al. 2016; Marshall et al. 2022). This research aims to advance the broader goal of mapping the C-H phase diagram under extreme conditions.

6.2 Methodology

Shock compression experiments on pre-compressed cyclohexane were conducted at the OMEGA EP laser facility using target configurations consisting of diamond or sapphire windows, our sample, and a quartz standard (Figure 3.2). The diamond/sapphire anvil cells were loaded with cyclohexane and pre-compressed to static pressures of 1.4 - 6.4 GPa. These were loaded at room temperature to solidify initial phases of cyclohexane and access off-principal Hugoniot states.

The targets incorporated Boehler-Almax diamond anvils (1.25 mm diameter, 0.39 mm height), or sapphire anvils (1.25 mm diameter, 0.5 mm height), mounted on tungsten carbide seats, with a 5 μm gold coating applied to enhance reflectivity for optical diagnostics. Ruby fluorescence provided our initial pressures through measurements of the R_1 line shift (Dewaele et. al., 2008), while the quartz standard served as an impedance matching reference for pressure and particle velocity determination (Brygoo et. al., 2015)

Two distinct laser pulse configurations were used to probe the high-pressure states of cyclohexane. The primary configuration used four UV beams with 800 μm distributed phase plates delivering a temporally shaped 10 ns pulse (SG99v001) at energies ranging from 1200 J to 4000 J. A secondary configuration employed a shorter 3 ns temporally shaped pulse to examine different compression timescales along the same energy range. These laser pulses ablated a CH foil to drive well-controlled shocks into the target assembly, allowing investigation of pressure-temperature conditions spanning 80-600 GPa and 5,000-30,000 K along off-principal Hugoniot paths.

The experimental diagnostics focused on two key measurement techniques. A velocity interferometer system for all reflectors (VISAR), which provides precise tracking of shock-front and interface motions, with the detailed methodology for these measurements described in Section 3.3.1. Simultaneously, streaked optical pyrometry (SOP) enabled temperature determination through analysis of thermal emission spectra, with the specific implementation outlined in Section 3.3.2. The shock velocities were then used to calculate pressure by way of the Rankine-Hugoniot relations, with quartz as the reference standard. SOP measurements employed

grey-body assumptions to derive temperature profiles (Gregor, et. al. 2016). This combined diagnostic characterizes cyclohexane's dynamic response under compression conditions relevant to both planetary science and high-energy-density physics applications.

6.3 Results

Preliminary results suggest that the response of cyclohexane under shock compression exhibits a similar trend to that reported in Barrios et. al.'s (2010) study on polypropylene (CH_2) (Figure 6.2), with a reduced slope above $U_p = 7 – 8$ km/s. The notable difference is the initial densities and material structure (ring vs. chain). The initial densities for cyclohexane were above 1.1 g/cc. While Barrios et. al.'s (2010) initial density was 0.9 g/cc. Cyclohexane's rings may influence the velocities reported, while its main CH_2 structures around the ring leads behavior resembling that of CH_2 plastic. The change in U_s - U_p slope at $U_p \cong 8$ km/s suggests that the ring structure of cyclohexane may undergo rearrangement or partial dissociation under these

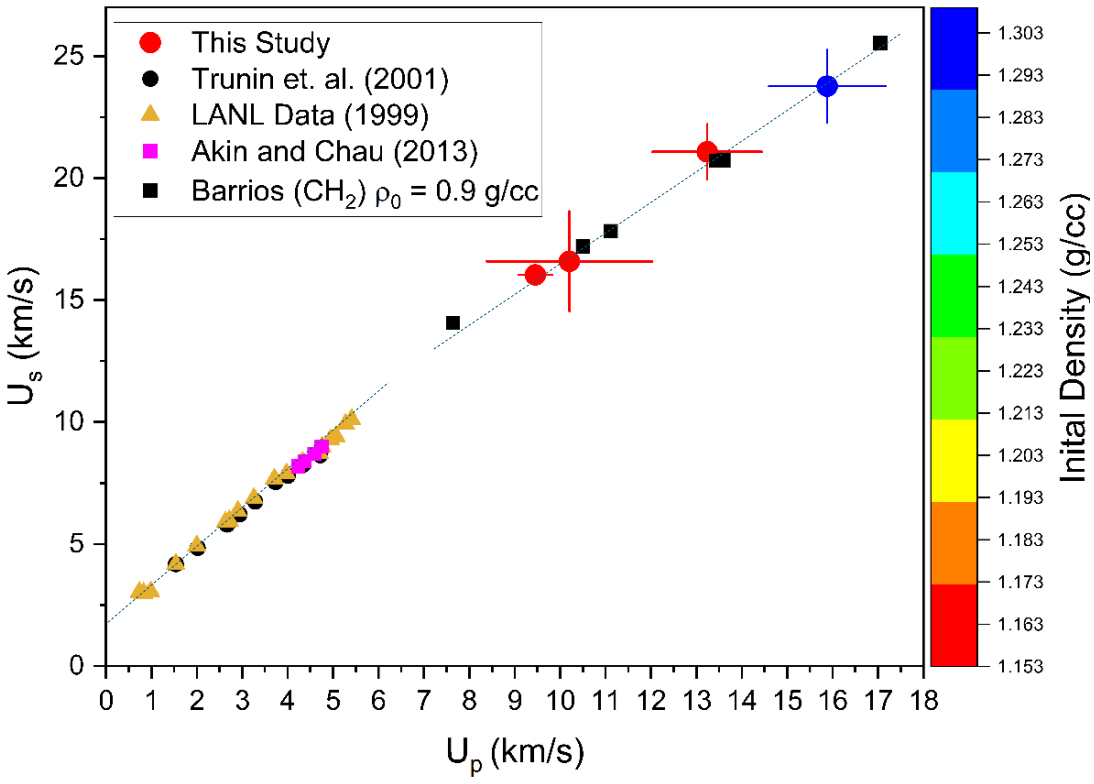

Figure 6.2. Shock velocity U_s versus particle velocity U_p, showing both previously published reference data and the current measurements for cyclohexane. Both U_s and U_p increase with increasing particle velocity. The present measurements on cyclohexane are in good agreement with those of Barrios et. al. (2010) on polypropylene (CH_2) ($\rho_0 = 0.9$ g/cc) at $U_p > 8$ km/s. The U_s- U_p kink evident in Figure 1.2 is present here at $U_p = 3.8 – 5$ km/s, but less obvious because of the scale of this plot. The dashed blue lines are there to denote the slope of each set of data points.

conditions, potentially leading to the formation of transient polymeric species or carbon clusters, as theorized for other carbon-hydrogen systems at extreme pressures (Weir et al. 1996; Celliers et al. 2018).

Additionally, results show an evolution in the optical properties of cyclohexane under dynamic compression. The reflectivity (Figure 6.3), while scattered, exhibits a general trend of increasing values with pressure above ~80 GPa. This trend is consistent with a gradual closure of the electronic band gap, a precursor to additional electronic changes (Celliers et al., 2018). Based on established correlations in simpler hydrocarbons, such a rise in reflectivity can be associated with the eventual onset of an insulator-to-conductor transition (ICT) at higher pressures (Barrios et al. 2010; Celliers et al. 2018).

These experimental conditions appear to be sufficient to rupture chemical bonds, with the observed trends signaling the initial stages of dissociation (Tabak et. al. 2024). While the current data makes it challenging to assign a specific transition pressure, the correlation between reflectivity and changes in EOS suggest that cyclohexane is progressing toward a dissociated, electronically degenerate state.

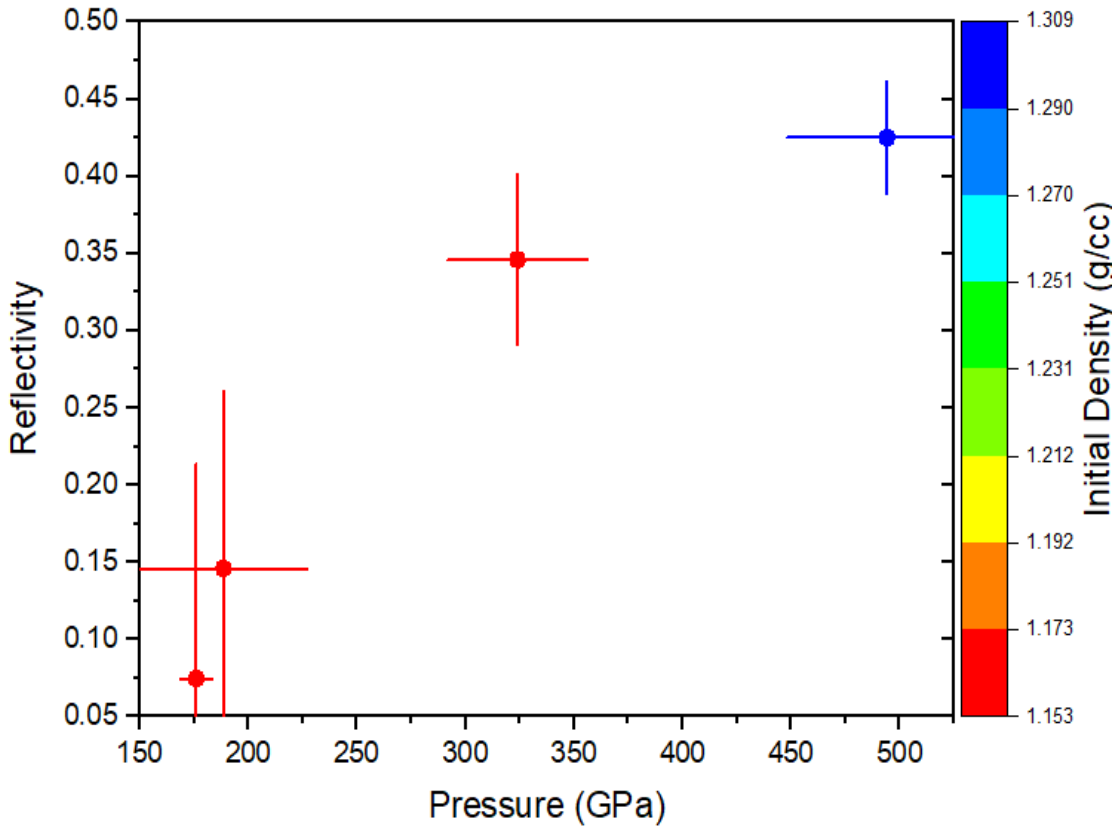

Figure 6.3. Reflectivity of cyclohexane as a function of pressure. Data points are color-coded according to the initial density of the sample. Current data shows that reflectivity increases with pressure.

Bibliography

Akaishi, M.; Shaji Kumar, M. D.; Kanda, H.; Yamaoka, S. Formation process of diamond from supercritical H_2O-CO_2 fluid under high pressure and high temperature conditions. *Diamond and Related Matrials* **2000** *9* (12), 1945-1950

Akin, M. C.; Chau, R. Dynamic compression of cyclohexane: Equation of state and dissociation behavior. *Journal of Applied Physics* **2013**, *113*, 183501.

Anderson, O.L., Isaak, D.G. and Yamamoto, S., Anharmonicity and the equation of state for gold. *Journal of Applied Physics*, **1989** *65*(4), pp.1534-1543.

Andriambariarijaona, L.; Datchi, F.; Zhang, H.; Beneut, K.; Baptiste, B.; Guignot, N., Ninet, S. High pressure-temperature phase diagram of ammonia hemihydrate. *Phys. Rev. B.* **2023** *108,* 174102

Antsyshkin, D.V., Dunaeva, A.N. & Kuskov, O.L. Thermodynamics of phase transitions in the system ice VI-Ice VII-water. *Geochem. Int.* **48**, 633–642 (2010).

Baraffe, I.; Chabrier, G.; Barman, T. Structure and evolution of Super-Earth to Super-Jupiter exoplanets: I. Heavy element enrichment in the interior. *Astronomy & Astrophysics* **2008**, *482*(1), 315–332.

Barrios, M. A.; Boehly, T. R.; Eggert, J. H.; Hicks, D. G.; Hamel, S.; Swift, D. C.; Collins, G. W. High-precision measurements of the equation of state of polystyrene (CH) to 70 Mbar. *Physics of Plasmas* **2010**, *17*, 056307.

Barker, L. M.; Hollenbach, R. E. Laser interferometer for measuring high velocities of any reflecting surface. *Journal of Applied Physics* **1972**, *43*, 4669.

Bassett, W.A.; Shen, A.H.; Bucknum, M.; Chou, I.M.A new diamond anvil cell for hydrothermal studies to 2.5 GPa and from− 190 to 1200° C. *Review of Scientific Instruments* **1993** *64*(8), 2340-2345.

Bastea, S. Nanocarbon condensation in detonation. *Scientific Reports* **2017**, *7*, 42151.

Batalha, N. M.; Rowe, J. F.; Bryson, S. T.; Barclay, T.; Burke, C. J.; Caldwell, D. A.; Christiansen, J. L.; Mullally, F.; Thompson, S. E.; Brown, T. M.; et al. Planetary candidates observed by Kepler. III. Analysis of the first 16 months of data. *Astrophysical Journal Supplement Series* **2013**, *204*, 24.

Bell, P.M.; Mao, H.K.; Xu, J.A. Error analysis of parameter-fitting in equations of state for mantle minerals. *High-Pressure Research in Mineral Physics: A Volume in Honor of Syun-iti Akimoto* **1987** *39*, 447-454.

Benedetti, L. R.; Loubeyre, P. High-pressure experiments: Techniques and results. *High Pressure Research* **2004**, *24*(4), 423–445.

Benedetti, L. R.; Nguyen, J. H.; Caldwell, W. A.; Liu, H.; Kruger, M.; Jeanloz, R. Dissociation of CH_4 at high pressures and temperatures: Diamond formation in giant planet interiors? *Science* **1999**, *286*, 100–102.

Bethkenhagen, M.; French, M.; Redmer, R. Equation of state and phase diagram of ammonia at high pressures from ab initio simulations. *Journal of Chemical Physics* **2013**, *138*, 234504.

Bethkenhagen, M.; Meyer, E.R., Hamel, S., Nettelmann, N., French, M., Scheibe, L., Ticknor, C., Collins, L. A., Kress, J. D., Fortney, J.J. Planetary Ices and the Linear Mixing Approximation *Astrophysical Journal* **2017**, *848*, 67.

Bezacier, L.; Caracas, R.; Thomas, C.; Perrillat, J.-P.; Cardon, H. Elasticity of ammonia dihydrate under pressure and implications for icy satellites. *Journal of Geophysical Research: Planets* **2014**, *119*, 1680–1688.

Birch, F. Finite elastic strain of cubic crystals. *Physical review* **1947** *71*(11), 809.

Boehler, R.; Zerr, A. High-pressure behavior of materials relevant to planetary interiors. *Science* **1994**, *265*, 723.

Boehler, R.; Zerr, A. Decomposition of alkanes at high pressures and temperatures. *Science* **1993**, *262*, 553–555.

Bolme, C. A.; Swift, D. C.; Elkin, V. M.; Cuneo, M. E.; Blue, B. E.; More, R. M. Measurement of Hugoniot data for CH materials. *Journal of Applied Physics* **2008**, *104*, 043504.

Boppart, H.; van Straaten, J.; Silvera, I. F. Raman spectra of diamond at high pressures. *Phys. Rev. B* **1985** *32*, 1423(R)

Boujibar, A.; Gillis-Davis, J.; Righter, K.; Danielson, L.; Nakamura-Messenger, K.; Fries, M. Hydrous silicates in planetary interiors: A possible source of buoyancy and magnetic anomalies. *Geophysical Research Letters* **2020**, *47*, e2020GL087876.

Bridgman, P,W., Physics of High Pressure. *London Bells and Sons* **1949**

Brygoo, S.; Loubeyre, P.; Occelli, F.; LeToullec, R. High-pressure diamond behavior. *Journal of Applied Physics* **2015**, *118*, 195901.

Campbell, A. J. Advances in diamond anvil cell techniques. *Review of Scientific Instruments* **2008**, *79*, 015108.

Cavazzoni, C.; Chiarotti, G. L.; Scandolo, S.; Tosatti, E.; Bernasconi, M.; Parrinello, M. Superionic and metallic states of water and ammonia at giant planet conditions. *Science* **1999**, *283*, 44–46.

Celliers, P. M.; Collins, G. W.; Da Silva, L. B.; Wallace, R. J.; Gold, D. M.; Foord, M. E.; Hammel, B. A.; Kilkenny, J. D.; Weber, S. V.; Cauble, R.; et al. Diagnostic applications of VISAR and SOP for simultaneous velocity and temperature measurements. *OMEGA Laser Facility* **2000**.

Ce

Celliers, P.; Millot, M.; Rygg, J. R.; et al. Insulator-metal transition in dense fluid deuterium. *Science* **2018**, *361*, 677–682.

Chau, R., Hamel, S. & Nellis, W. Chemical processes in the deep interior of Uranus. *Nat Commun* **2011** *2*, 203

Cheng, B., Hamel, S. & Bethkenhagen, M. Thermodynamics of diamond formation from hydrocarbon mixtures in planets. *Nat Commun* **2023** *14*, 1104

Connerney, J. E. P.; Acuña, M. H.; Ness, N. F. The magnetic field of Uranus. *Journal of Geophysical Research* **1987**, *92*, 15329–15336.

Conway, L.J.; Pickard, C. J.; Hermann, A. Rules of formation of H-C-N-O compounds at high pressure and the fates or planetary ices. *Proc. Natl. Acad. Sci. U.S.A.* **2021** *118* (19) e2026360118,

Dewaele A., Torrent M., Loubeyre P. and Mezouar M. Compression curves of transition metals in the Mbar range: Experiments and projector augmented-wave calculations **2008** *Phys. Rev. B* 78, 104102

Dolan, D. Foundations of VISAR analysis. *Technical Report*, Sandia National Laboratories **2006**.

Du, Z.; Amulele, G.; Benedetti, L. R.; Lee, K. K. M. Experimental techniques for high-pressure studies. *Review of Scientific Instruments* **2013**, *84*, 075111.

Eggert, J. H.; Hicks, D. G.; Rygg, J. R.; et al. Melting temperature of diamond at ultrahigh pressure. *Nature Physics* **2010**, *6*, 40–43.

Fischer, R. A.; Campbell, A. J. The effect of pressure on the physical properties of planetary materials. *American Mineralogist* **2010**, *95*, 1473–1477.

Fortes, A. D.; Wood, I. G.; Grigoriev, D.; Alfredsson, M.; Vocadlo, L.; Knight, K. S. The high-pressure phase diagram of ammonia dihydrate. *Icarus* **2009**, *202*, 345–357.

Fortney, J. J.; Nettelmann, N. The interior structure, composition, and evolution of giant planets. *Space Science Reviews* **2010**, *152*(1–4), 423–447.

Guarguaglini, M., Hernandez, JA., Okuchi, T. *et al.* Laser-driven shock compression of "synthetic planetary mixtures" of water, ethanol, and ammonia. *Sci Rep* **2019** 9, 10155

Gao, G.; Oganov, A. R.; Ma, Y.; Wang, H.; Li, P.; Li, Y.; Cui, T. High-pressure crystal structures and superconductivity of hydrides of sulfur, selenium, and tellurium. *Proceedings of the National Academy of Sciences* **2010**, *107*, 1317–1320.

Geballe, Z. M.; Jeanloz, R. Origin of temperature plateaus in laser-heated diamond anvil cell experiments. *Journal of Applied Physics* **2012**, *111*, 123518.

Ghosh, D. B.; Bajgain, S. K.; Mookherjee, M.; Karki, B. B. Carbon-bearing silicate melt at deep mantle conditions. *Scientific Reports* **2017** *7: 848*

Gregor, M. C.; Boni, R.; Sorce, A.; Kendrick, J.; McCoy, C. A.; Polsin, D. N.; Boehly, T. R.; Celliers, P. M.; Collins, G. W.; Fratanduono, D. E.; Eggert, J. H.; Millot, M. Absolute calibration of the OMEGA streaked optical pyrometer for temperature measurements of compressed materials. *Review of Scientific Instruments* **2016** *87*(11).

Guillot, T. Interiors of Giant Planets Inside and Outside the Solar System. **1999** *286* (5437), 72-77

Guillot, T. The interiors of giant planets: Models and outstanding questions. *Annual Review of Earth and Planetary Sciences* **2005**, *33*, 493–530.

Guillot, T.; Gautier, D. 10.16 – Giant Plantes (ed. Schuber, G. Treatise on Geophysics) *Elsevier* **2015**, 529-557

Hartley, N.; McWilliams, R. S.; et al. Phase separation and diamond precipitation in laser-compressed hydrocarbons. *Physical Review Letters* **2018**, *121*, 245501.

He, Z.; Rödel, M.; Lütgert, J.; Bergermann, A.; Bethkenhagen, M.; Chekrygina, D.; Cowan, T. E.; Descamps, A.; French, M.; Galtier, E.; et al. Diamond formation kinetics in shock-compressed C–H–O samples. *Science Advances* **2022**, *8*, eabo0617.

Heinz, D. L.; Jeanloz, R. Measurement of the melting curve of Mg0.9Fe0.1SiO3 at lower mantle conditions and its geophysical implications *Journal of Geophysical Research* **1987**, *92*(B11), 11437–11444.

Helled, R.; Anderson, J. D.; Podolak, M.; Schubert, G. Interior models of Uranus and Neptune. *The Astrophysical Journal* **2011** *726,* 15

Helled R, Guillot T. Interior models of Saturn: including the uncertainties in shape and rotation. *The Astrophysical Journal.* **2013** *767*(2), 113

Helled, R.; Stevenson, D; The Fuzziness of Giant Planets' Cores. *The Astrophysical Journal*. **2017** *840:L4*

Helled, R.; Fortney, J. J. The interiors of Uranus and Neptune: Current understanding and open questions. *Philosophical Transactions of the Royal Society A* **2020**, *378*, 20190474.

Heyne, J. S.; Dooley, S.; Serinyel, Z.; Dryer, F. L.; Curran, H. Decomposition Studies of Isopropanol in a Variable Pressure Flow Reactor *Zeitschrift für Physikalische Chemie*, **2015** *229* (6) 881-907

Hirai, H.; Konagai, K.; Kawamura, T.; Yamamoto, Y.; Yagi, T. Polymerization and diamond formation from melting methane and their implication in ice lay of giant planets. **2009** *174* (1-4), 242-246

Hirose, K.; Fei, Y.; Ma, Y.; Mao, H. K. The fate of subducted basaltic crust in the Earth's lower mantle. *Nature* **1999**, *397*, 53–56.

Holmes, N.C.; Moriarty, J.A.; Gathers, G.R.; Nellis, W.J., The equation of state of platinum to 660 GPa (6.6 Mbar). *Journal of Applied Physics*, **1989** *66*(7), pp.2962-2967

Hubbard, W. B. The interior of Neptune. *Journal of Geophysical Research* **1980**, *85*, 225–234.

Hubbard, W.B.; Nellis, W.J.; Mitchell, A.C.; Holmes, N.C.; Limaye, S.S.; McCandless, P.C., Interior structure of Neptune: comparison with Uranus. *Science*, **1991** *253*(5020), pp.648-651.

Howe, A. R.; Burrows, A.; Verne, W. Mass-radius relations and core-envelope decompositions of Super-Earths and Sub-Neptunes. *Astrophysical Journal* **2014**, *787*(2), 173.

Jeanloz, R., Celliers, P.M., Collins, G. W., Eggert, J. H., Lee, K. K. M., Lee, R.S., McWilliams, R. S., Brygoo, S., & Loubeyre, P., Achieving high-density states through shock-wave loading of precompressed samples, *Proc. Natl. Acad. Sci. U.S.A.* 2004, 104 (22) 9172-9177

Jeanloz, R.; Kavner, A. Melting criteria and imaging spectroradiometry in laser-heated diamond-cell experiments. *Philosophical Transactions of the Royal Society A* **1996**, *354*(1711), 1279–1305.

Jayaraman, A. Diamond anvil cell and high-pressure studies. *Reviews of Modern Physics* **1983**, *55*(1), 65–108.

Kadobayashi, H.; Hirai, H.; Ohfuji, H.; Ohtake M.; Muraoka, M.; Yoshida, S.; Yamamoto, Y. Structural evolution of methane hydrate under pressures up to 134 GPa. *J. Chem. Phys.***2020**; *152* (19): 194308

Kadobayashi, H., Ohnishi, S., Ohfuji, H. *et al.* Diamond formation from methane hydrate under the internal conditions of giant icy planets. *Sci Rep* **2021** *11*, 8165.

Khazaei, M.; Tripathi, M. N.; Kawazoe, Y. First-principles simulation of cyanogen under high pressure: Formation of paracyanogen and an insulating carbon nitride solid *Phys. Rev. B* **2011** *83*, 134111

Klotz, S.; Komatsu, K.; Kagi, H.; Kunc, K.; Sano-Furukawa, A.; Machida, S.; Hattori, T., Bulk moduli and equations of state of Ice VII and Ice VIII. *Physical Review B*, **2017** *95*(17), p.174111

Knudson, M. D.; Desjarlais, M. P. The shock compression response of water to 700 GPa. *Journal of Applied Physics* **2009**, *105*(10), 103532.

Kraus, D.; Ravasio, A.; Gauthier, M.; Gericke, D. O.; Vorberger, J.; Frydrych, S.; Fletcher, L. B.; Schuster, A. K.; Doppner, T.; Lee, H. J.; et al. Formation of diamonds in laser-compressed hydrocarbons at planetary interior conditions. *Nature Astronomy* **2017**, *1*, 606–611.

Kraus, D.; et al. Shock-compression experiments on hydrocarbons up to megabar pressures. *Physical Review Research* **2023**, *5*, 023201.

Kunz, K.; Yan, J.; Cornell, E.; Domning, E. E.; Yen, C. E.; Doran, A.; Beavers, C. M.; Treger, A.; Willimans, Q.; MacDowell, A. A., Implementation and application of the peak scaling method for temperature measurement in the laser heated diamond anvil cell. *Rev. Sci. Instrum.* **2018**; *89* (8): 083903.

Li, Z.-G.; Chen, Q.-F.; Gu, Y.-J.; Zheng, J. C. Hugoniot measurements of hydrocarbons and the equation of state of polystyrene to 200 GPa. *AIP Advances* **2016**, *6*, 105309.

Lindal, G. F.; Lyons, J. R; Sweetnam, D. N.; Eshleman, V. R.; Hinson, D. P.; Tyler, G. L. The atmosphere of Uranus: Results of radio occultation measurements with Voyager 2. **1987** *92* (A13), 14987-15001

Lobanov, S. S.; Pei-Nan, C.; Chen, X.; Chang-Sheng Z.; Konstantin, D. L.; Ho-Kwang, M.; Goncharov, A. F. Carbon precipitation from heavy hydrocarbon fluid in deep planetary interiors. *Nature Communications.* **2013** *4*(1), 2446

Lorenzen, W.; Becker, A.; Redmer, R. Progress in Warm Dense Matter and Planetary Physics. In: Graziani, F., Desjarlais, M., Redmer, R., Trickey, S. (eds) Frontiers and Challenges in Warm Dense Matter. *Lecture Notes in Computational Science and Engineering,* **2014** *96*. Springer, Cham.

Loubeyre, P.; LeToullec, R.; Hausermann, D.; Hanfland, M.; Hemley, R.J.; Mao, H.K; Finger, L.W. X-ray diffraction and equation of state of hydrogen at megabar pressures. *Nature* **1996** *383*(6602), 702-704.

Lyon, F.; Johnson, V. J. Compilation of Hugoniot data. *Technical Report* **1992**, Los Alamos National Laboratory.

Ma, C.; Li, F.; Zhou, Q.; Huang, F.; Wang, J.; Zhang, M.; Wang, Z.; Cui, Q.; Ammonia molecule rotation of pressure-induced phase transition in ammonia hemihydrates $2NH_3 \cdot H_2O$, *RSC Adv.,* **2012**, *2*, 4920–4924.

Madhusudhan, N.; Lee, K. K. M.; Mousis, O. A Possible Carbon-Rich Interior in Super-Earth 55 Cancri e. *The Astrophysical Journal* **2012** I758:36

Marshall, M.; Swift, D. C.; Kraus, R. G.; Bolme, C. A.; Celliers, P. M.; Millot, M.; Fratanduono, D. E.; Collins, G. W.; Eggert, J. H. Shock-compression and sound velocity measurements on polystyrene to 200 GPa. *Journal of Applied Physics* **2022**, *131*(1), 015902.

Mao, H.K.; Bell, P.M.; Shaner, J.T.; Steinberg, D.J. Specific volume measurements of Cu, Mo, Pd, and Ag and calibration of the ruby R 1 fluorescence pressure gauge from 0.06 to 1 Mbar. *Journal of applied physics* **1978** *49*(6), 3276-3283.

Mao, H.K.; Xu, J.A.; Bell, P.M. Calibration of the ruby pressure gauge to 800 kbar under quasi-hydrostatic conditions. *Journal of Geophysical Research: Solid Earth* **1986** *91*(B5), 4673-4676.

Merrill, L.; Bassett, W.A. Miniature diamond anvil pressure cell for single crystal x-ray diffraction studies. *Review of Scientific Instruments* **1974** *45*(2), 290-294.

McWilliams, R.S., Spaulding, D.K., Eggert, J.H., Celliers, P.M., Hicks, D.G., Smith, R.F., Collins, G.W. and Jeanloz, R., Phase transformations and metallization of magnesium oxide at high pressure and temperature. *Science* **2012** *338*(6112) 1330-1333.

Millot, M.; Coppari, F.; Rygg, J. R.; Barrios, A. C.; Hamel, S.; Swift, D. C.; Eggert, J. H. Nanosecond X-ray diffraction of shock-compressed superionic water ice. *Nature* **2018**, *569*(7756), 251–255.

Montoya, J. A.; Goncharov, A. F. High-pressure behavior of simple hydrocarbons studied by Raman spectroscopy. *Journal of Applied Physics* **2012**, *111*(11), 112617.

Nettelmann, N.; Helled, R.; Fortney, J. J.; Redmer, R. New indication for a dichotomy in the interior structure of Uranus and Neptune from their evolution. *Planetary and Space Science* **2013**, *77*, 143–151.

National Academies of Sciences, Engineering, and Medicine. *Origins, Worlds, and Life: A Decadal Strategy for Planetary Science and Astrobiology 2023-2032*. **2023** Washington, DC: The National Academies Press.

Naumova, A. S.; Lepeshkin, S. V.; Bushlanov, P. V.; Oganov, A. R. Unusual chemistry of the C–H–N–O system under pressure and implications for giant planets. *Journal of Physical Chemistry A* **2021**, *125*(18), 3936–3942.

Nellis, W. J.; Homes, N. C.; Mitchell, A. C.; Hamilton, D. C.; Nicol, M. Equation of state and electrical conductivity of "synthetic Uranus," a mixture of water, ammonia, and isopropanol, at shock pressure up to 200 GPa (2 Mbar). *J. Chem. Phys.* **1997** *107* (21): 9096–9100

Nellis, W. J.; Hamilton, D. C.; Holmes, N. C.; Radousky, H. B.; Ree, F. H.; Mitchell, A. C.; Nicol, M. The nature of the interior of Uranus based on studies of planetary ices at high dynamic pressure. *Science* **1988**, *240*(4853), 779–781.

Nettelmann, N.; Helled, R.; Fortney, J. J.; Redmer, R. *New indication for a dichotomy in the interior structure of Uranus and Neptune from the application of modified shape and rotation data.* Planetary and Space Science, 2013, **77**, 143–151

O'Bannon, E. F., Jenei, Z., Cynn, H., Lipp, M. J.; Jeffries, J. R. Contributed Review: Culet diameter and the achievable pressure of a diamond anvil cell: Implications for the upper pressure limit of a diamond anvil cell. *Rev. Sci. Instrum.* **2018**, *89*, 111501

Occelli, F.; Loubeyre, P.; LeToullec, R. Properties of diamond under hydrostatic pressures up to 140 GPa. *Nature Materials* **2003**, *2*(3), 151–154.

Orth, C. D. New multiphase equation of state for carbon at extreme conditions. *Physics of Plasmas* **2016**, *23*, 122712.

Pearl, J. C.; Conrath, B. J.; Hanel, R. A.; Pirraglia, J. A.; Coustenis, A. The albedo, effective temperature, and energy balance of Uranus, as determined from Voyager IRIS data. *Icarus* **1990** *84* (1), 12-28

Pearl, J. C.; Conrath, B. J. The albedo, effective temperature, and energy balance of Neptune, as determined from Voyager data. *J. Geophys. Res. Space Physics* **1991** *96* (S01), 18921-18930

Piermarini, G. J.; Block, S.; Barnett, J. D.; Forman, R. A. Calibration of the pressure dependence of the R_1 ruby fluorescence line to 195 kbar. *J. Appl. Phys.* **1975** *46,* 2774-2780

Podolak, M.; Helled, R.; Schubert, G. Effect of non-adiabatic thermal profiles on the inferred compositions of Uranus and Neptune. *Monthly Notices of the Royal Astronomical Society* **2019**, *487*(2), 2653–2664.

Prescher, C.; Prakapenka, V. B. DIOPTAS: A program for reduction of two-dimensional X-ray diffraction data and data exploration. *High Pressure Research* **2015**, *35*(3), 223–230.

Rafter, S. E.; Kaspi, S.; Chelouche, D.; Sabach, E.; Karl, D.; Behar, E. Reverberation mapping of a low-mass black hole in a narrow-line Seyfert 1 galaxy. *Astrophysical Journal* **2013**, *773*(1), 24.

Redmer, R.; Mattsson, T. R.; Nettlemann, N.; French, M. The phase diagram of water and the magnetic fields of Uranus and Neptune. **2011** *211* (1), 798-803

Ree, F. Shock-induced dissociation and ionization of hydrocarbons. *Journal of Chemical Physics* **1979**, *70*, 974–983.

Remington, B.A., Allen, P., Bringa, E.M. Hawreliak, J.; Ho D.; Lorenz, K.T.; Lorenzana, H.; Mcnaney, J.M.; Meyers, M.A.; Pollaine, S.W.; Rosolankova, K. Material dynamics under extreme conditions of pressure and strain rate. *Materials Science and Technology* **2006** *22*(4), 474-488.

Robinson, V. N.; Wang, Y.; Ma, Y.; Hermann, A. Stabilization of ammonia-rich hydrate inside icy planets, *Proc. Natl. Acad. Sci. U.S.A.* **2017** *114* (34) 9003-9008

Santoro, M., Gorelli, F.A., Dziubek, K., Scelta, D. and Bini, R. (2020). Structural and Chemical Modifications of Carbon Dioxide on Transport to the Deep Earth. In Carbon in Earth's Interior (eds C.E. Manning, J.-F. Lin and W.L. Mao)

Seifter, A.; Swift, D.C., Pyrometric measurement of the temperature of shocked molybdenum. *Phys. Rev. B* **2008** *77*, 134104

Scheibe, L.; Nettelmann, N.; Redmer, R. Thermal evolution of Uranus and Neptune: I. Adiabatic models. *Astronomy & Astrophysics* **2019**, *632*, A70.

Sharma, S.K., Mao, H.K., Bell, P.M. and Xu, J.A., Measurement of stress in diamond anvils with micro-Raman spectroscopy. *Journal of Raman Spectroscopy* **1985** *16*(5) 350-352.

Sherman, W.; Militzer, B.; Hubbard, W. B. Ab initio equations of state for hydrogen-helium mixtures with recalibration of the giant planet mass-radius relation. *Physical Review B* **2012**, *86*(22), 224102.

Shen, G.; Lazor, P. Measurement of melting temperatures of some minerals under lower mantle pressures. *Journal of Geophysical Research* **1995**, *100*(B9), 17699–17713.

Soyuer, D.; Kraus, D.; Ravasio, A.; et al. Diamond precipitation kinetics in laser-compressed hydrocarbons. *Monthly Notices of the Royal Astronomical Society* **2020**, *498*, 5373–5385.

Stanley S.; Bloxham J. Numerical dynamo models of Uranus' and Neptune's magnetic fields. *Icarus*. **2006**, *184*(2), 556-72.

Stevenson, D. J. Cosmochemistry and structure of the giant planets and their satellites. **1985**, *62* (1), 4-15

Tabak, G.; McWilliams, R. S.; et al. Kinetics of diamond formation from hydrocarbons at planetary interior conditions. *Physical Review B* **2024**, *109*, 094105.

Trunin, R. F. Shock compression of condensed materials at high pressures: Data compilation. *Sarov* **2001**.

Tschauner, O.; Huang, S.; Greenberg, E.; Parakapenka, V. B.; Ma, C.; Rossman, G. R.; Shen, A. H.; Zhang, D.; Newville, M.; Lanzirotti, A.; Tait, K. Ice-VII inclusions in diamonds: Evidence for aqueous fluid in Earth's deep mantle. *Science* **2018** *359*,1136-1139

Valencia, D.; Sasselov, D. D.; O'Connell, R. J. Radius and structure models of the first super-Earth planet. *Astrophysical Journal* **2007**, *656*(1), 545–551.

Vazan, A.; Ormel, C. W.; Noack, L.; Dominik, C. Contribution of the core to the thermal evolution of sub-Neptunes. *Astrophysical Journal* **2018**, *869*(2), 163.

Vereshchagin, L. F.; Fateeva, N. S.; Magnitskaya, M. V. High-pressure studies of nitrogen and methane. *JETP Letters* **1975**, *22*(4), 106–108.

Weir, S. T.; Mitchell, A. C.; Nellis, W. J. Metallization of fluid molecular hydrogen at 140 GPa. *Physical Review Letters* **1996**, *76*, 1860–1863.

Werellapatha, K.; Tran, T.; Remington, B. A.; Swift, D. C. VISAR measurements of shocked hydrocarbons. *Review of Scientific Instruments* **2021**, *92*(5), 053903.

Williams, Q.; Knittle, E.; Jeanloz, R. The high-pressure melting curve of iron: Implications for the Earth's core. *Journal of Geophysical Research* **1991**, *96*, 2171–2184.

Wilson, H. F.; Militzer, B. Solubility of water ice in metallic hydrogen: Consequences for core erosion in gas giant planets. *Astrophysical Journal* **2012**, *745*, 54.

Yang, L.; Karandikar, A.; Boehler, R. High-pressure melting curve of iron and phase transitions. *Review of Scientific Instruments* **2012**, *83*(6), 063905.

Zaghoo, M.; Husband, R. J.; Silvera, I. F. Observation of the insulator-metal transition in dense fluid deuterium. *Physical Review Letters* **2019**, *122*, 195001.

Zel'Dovich, Y.B.; Raizer, Y.P. *Physics of shock waves and high-temperature hydrodynamic phenomena*. **2002** Courier Corporation.

Zerr, A.; Serghiou, G.; Boehler, R.; Ross, M. Decomposition of alkanes at high pressures and temperatures. *High Pressure Research* **2006**, *26*, 23–29.

Appendix A.

4-Color Laser Heating and Melting Point Determination of Various Metals

A.1 Background on 4-Color Laser Heating System

The study of melting under high-pressure and high-temperature conditions provides insights into thermodynamic phase stability, planetary differentiation, and materials design. The laser-heated Diamond Anvil Cell remains an effective tool for achieving the simultaneous pressure–temperature regimes necessary to explore such behavior.

Accurately identifying the melting point of materials in the Diamond Anvil Cell environment presents unique challenges due to steep thermal gradients, chemical reactivity, and limited time and spatial resolution during heating. To address these challenges, Du et al. (2013) developed a technique that combines two-dimensional, four-color multi-wavelength imaging radiometry with short-duration laser flash heating. This system enables spatially resolved temperature measurements across a laser-induced hotspot. Its integration with post-experiment scanning electron microscopy (SEM) offers a method for identifying melt textures and correlating them with localized thermal data.

Previous studies have relied on a variety of indirect proxies for detecting melting in high-pressure experiments, including changes in laser power–temperature slopes (Hirose et al., 1999; Shen & Lazor, 1995), thermal emission behavior (Fischer & Campbell, 2010), and quench texture observations (Heinz & Jeanloz, 1987; Boehler & Zerr, 1993). However, these approaches are often subject to interpretation and can be challenged by thermal runaway, fluid motion, or emissivity changes unrelated to melting (Jeanloz & Kavner, 1996; Geballe & Jeanloz, 2012).

The approach described by Du et al. (2013) addresses these issues by producing high-resolution, time-resolved thermal maps during laser heating and directly correlating them with quenched morphological features. This method has been successfully validated using several metals at ambient and high pressures, demonstrating agreement with established melting temperature values (Yang et al., 2012).

In the present study, we apply the Du et al. (2013) system to further investigate the melting behavior of metals both at ambient pressure and across a range of pressure conditions. Our goal is to leverage the combined advantages of flash heating, multi-wavelength radiometry, and SEM-based texture analysis to better constrain melting temperatures in materials where previous measurements have been sparse, uncertain, or inconsistent. By conducting multiple flash-heating experiments above and below the anticipated melting point and superimposing SEM-identified melt blebs onto temperature maps, we can delineate melt boundaries and estimate uncertainties associated with thermal gradients, spatial resolution, and possible superheating effects.

This approach provides a pathway to expanding the database of high-pressure melting temperatures using a well-calibrated and reproducible experimental framework. The emphasis on morphological confirmation of melting, rather than reliance on indirect indicators, offers greater confidence in phase boundary determination. Our findings will contribute to the growing body of high-pressure melting data and demonstrate the continued utility of the Du et al. (2013) methodology for quantitative melt detection across a variety of metallic systems. Currently, this project is only in its early stages. With continuous updates to the system and a large variety of metals to test we are constrained in our data collection.

A.2 Current and Ongoing work (including updates to the system)

We conducted high-temperature laser heating experiments using our in-house four-color laser system, designed for studies of melting in metallic foils. The primary heating source was a 1070 nm infrared laser, aligned using a red laser on both sides of the sample to ensure beam overlap at the target.

Our experiments focused on (Rhenium (Re), Chromium (Cr), Cobalt (Co), Gold (Au), Hafnium (Hf), Iron (Fe), Aluminum (Al), Zirconium (Zr), Nickel (Ni), Palladium (Pd), Silver (Ag), Copper (Cu), Titanium (Ti), Vanadium (V), and Molybdenum (Mo)), which were purchased (*GoodFellow, Alfa Aesar*), as thin foils ranging from 0.1 mm to 0.5 mm in thickness. To ensure a flat, well-defined heating surface, each foil was pre-indented using a Diamond Anvil Cell equipped with 300–500 μm culets.

The indented samples were then placed in a custom-built sample holder and sealed with Kapton tape, with a small hole (~1 mm diameter) cut in the tape to expose only the metal foil to direct laser irradiation. Argon gas was then introduced into the chamber to create an inert atmosphere and minimize oxidation during laser heating.

Flash heating was carried out by pulsing the laser onto the metal foil for approximately 10 milliseconds at varying power levels. During this brief interval, the light intensity emitted from the heated spot was captured using a synchronized camera system, producing a single-frame image corresponding to the thermal state of the sample at peak heating.

These images were then processed using a custom analysis code to generate a temperature map of the laser-heated region. Following the heating experiments, the foils were examined using Scanning Electron Microscopy (SEM), focusing on the melt spot that typically measured 20–40 μm across. The SEM image was aligned with the corresponding temperature map, allowing us to pinpoint the location of melting by correlating the thermal and morphological data. The edge of the melt feature in the SEM image was used to define the melting boundary, and the corresponding temperature at that location was taken as the material's melting point. An example of this correlation process is shown in Figure A.1.

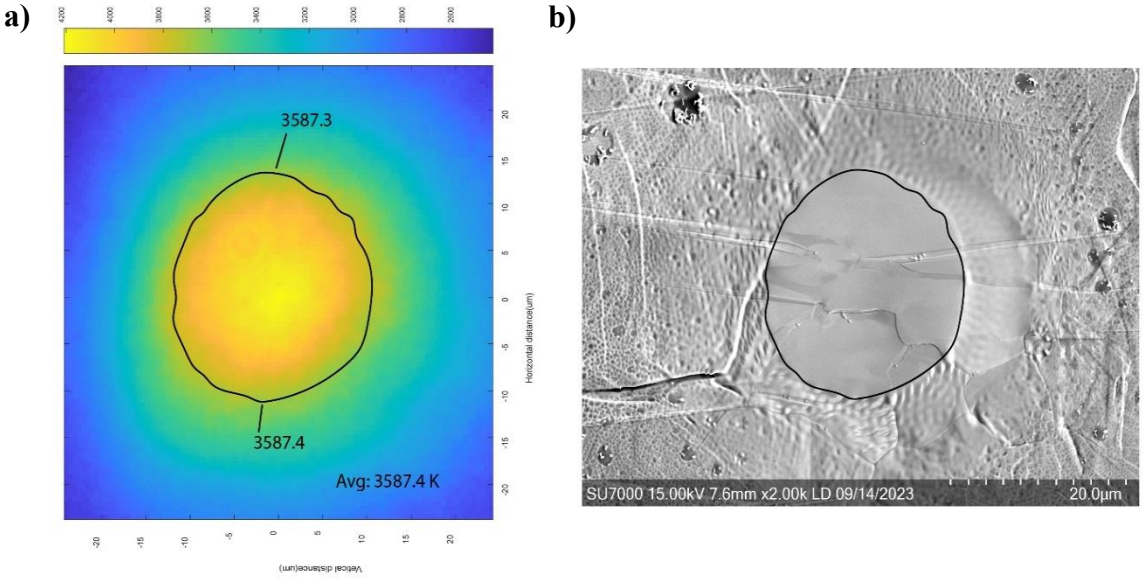

Figure A.1. (a) Temperature map calculated from analyzing the hot spots formed during heating. (b) Scanning Electron microscope (SEM) image of the hot spot on the Rhenium foil. The black like outlines the outer rim of the hot spot and is superimposed onto the temperature map (rotated to match orientation). The texture on the outer ring is the melt bleb. This is where the melting temperature is determined.

Several updates were made to both the laser system and the analysis workflow to improve reliability and data quality. To enhance optical monitoring, we installed 90/10 beam splitters in the beam path, which allows continuous visualization of the sample surfaces from both sides during alignment and heating, while still delivering 90% of the laser light to the target. Additionally, the system was configured to enable optional video recording of experiments for more detailed post-experiment review. With data processing, the analysis code was updated to improve calibration accuracy by subdividing each color channel into finer spatial intervals, allowing a more precise alignment of the 4-color images and therefore an improvement of the system's spectral response calibration. This refinement was then applied to the temperature analysis, and a smoothing routine was incorporated to produce clearer, more interpretable temperature maps of the melt region.

Appendix B: Estimating the Gravitational Energy Released by Diamond Sedimentation in Ice Giants

Estimating the gravitational potential energy released by diamond sedimentation provides a useful framework for evaluating how carbon differentiation could influence the long-term thermal evolution of ice giant planets. This calculation rests on several assumptions regarding the interior structure of Uranus-like planets. For example, the proportion of carbon available for sequestration as diamond, and the physical properties of the relevant materials. While simplified, this model offers first-order constraints on the magnitude of energy storage and release.

The parameters summarized in Table B.1 reflect the best available estimates from planetary structure models and experimental measurements of phase densities under high pressure and temperature. The mantle mass estimate draws on interior models of Uranus by Helled and Guillot (2013) and Redmer et al. (2011). The gravitational acceleration is approximated for mid-mantle depths as discussed by Podolak et al. (2019).

The density of diamond and surrounding fluids is based on high-pressure equations of state reported in Bethkenhagen et al. (2017) and Millot et al. (2019). The fraction of carbon settling out (f_s) is treated parametrically. The concentration of carbon within our Synthetic Uranus system was experimentally estimated to be ~10% by mass. Although this is higher than estimates for Uranus, which typically suggest a few percent carbon (Helled et al., 2020), we adopt this concentration as an upper bound scenario for the purpose of evaluating the maximum potential energy release from a Sythetic Uranus-like mantle.

Table B.1. Values and variables used within the calculation of energy released from the settlement of carbon in the ratios present in Synthetic Uranus.

Parameter	Symbol	Value	Reference
Mass fraction of carbon in mantle	f_C	0.107	Nellis et al. (1997), Synthetic Uranus
Estimated mantle mass of Uranus	M	3.5×10^{26} kg	Helled & Guillot (2013); Redmer et al. (2011)
Gravitational Acceleration	g	10 m/s^2	Podolak et al., (2019)
Settling Distance	h	10^7 m	Bethkenhagen et al., (2017)
Density of Diamond	ρ_d	3,500 kg/m^3	Bethkenhagen et al. (2017)
Density of mantle	ρ_{mantle}	1,500 kg/m^3	Bethkenhagen et al. (2017)

The vertical distance, over which diamond is assumed to settle, was set at 10^7 meters (10,000 kilometers), reflecting the approximate thickness of the mid-mantle region in which diamond would be denser than the surrounding fluid ices and would therefore experience net negative buoyancy (Bethkenhagen et al., 2017). The density of diamond under mantle conditions was taken as 3,500 kilograms per cubic meter, while the bulk density of the surrounding H_2O-rich ices was approximated at 1,500 kilograms per cubic meter, consistent with high-pressure phase behavior measured in diamond anvil cell experiments (Millot et al., 2019; Bethkenhagen et al., 2017). The effective density contrast, which determines the buoyancy-corrected gravitational force, is thus 2,000 kilograms per cubic meter.

The energy released by sedimentation arises because the dense diamond grains descend through the less dense mantle, converting gravitational potential energy into heat. This process can be quantified by the equation:

$$E = mgh\,(1 - \frac{\rho_{mantle}}{\rho_d})$$

where m is the mass of carbon sequestered as diamond, g is gravitational acceleration, h is the vertical distance of settling, ρ_d is the density of diamond, and ρ_{mantle} is the density of the mantle material it displaces.

Applying the above parameters, the total mass of carbon available for differentiation is computed as:

$$M_C = f_C * M = 0.10 * (3.5 * 10^{26}\ kg) = 3.5 *\ 10^{25}\ kg$$

Substituting into the energy equation yields:

$$E = (3.5 *\ 10^{25}\ kg\ ) * 10\frac{m}{s^2} * 10^7 m * (1 - \frac{1500\ kg/m^3}{3500\ kg/m^3})$$

where the density ratio simplifies to approximately 0.571. This gives:

$$E = (3.5 *\ 10^{25}\ kg) * 10^8 \frac{m^2}{s^2} * 0.571 = 2 *\ 10^{33}\ J$$

This value represents an upper bound, in which all carbon simultaneously precipitates as diamond and settles through the entire mantle thickness. Recognizing that in natural systems, only a fraction of carbon may differentiate over shorter timescales and smaller spatial intervals, we also considered more conservative scenarios. For instance, if only 10% of the carbon segregates episodically or the effective settling distance is closer to 10^6 meters rather than 10^7 m, the total energy is reduced by approximately an order of magnitude in each case, yielding values around ~10^{32} J. If both factors apply simultaneously, the energy would be reduced by two orders of magnitude, approaching ~10^{31} J. Even these lower estimates represent significant contributions to the internal energy budget, especially when compared to Uranus's observed low intrinsic heat flux, which implies total thermal losses on the order of 10^{20} J/yr (Pearl et al., 1990).

The relevance of this process to planetary evolution lies in the timescale and periodicity of sedimentation. If diamond forms intermittently and settles in discrete plumes, the associated energy release could occur in pulses, modulating the thermal gradient and potentially driving localized convection or influencing magnetic field generation (Stanley & Bloxham, 2006). Furthermore, the persistence of diamonds upon decompression, as observed in our experiments, suggests that once carbon is locked into crystalline form, it may remain sequestered for geological timescales, thereby contributing to compositional stratification and further inhibiting efficient convective overturn (Redmer et al., 2011; Bethkenhagen et al., 2017).

In summary, while this model simplifies the complex physics of planetary interiors, it demonstrates that carbon differentiation through diamond sedimentation is a plausible mechanism capable of releasing gravitational potential energy. Incorporating this process into future thermal evolution models may help reconcile the observed thermal anomalies of Uranus and Neptune with their internal compositions. Though, it should be noted that this calculation did not consider differences in mantle differentiation or variations in heterogeneity.

B.1 Reproduction of Energy Release by Bennedetti et al. (1999)

The previous section presented a simplified calculation of gravitational potential energy released by diamond sedimentation, assuming a uniform mantle composition containing 10% carbon by mass and treating the process as the descent of a slab of dense material through a

constant gravitational field over a representative mantle thickness. While this approach provides an accessible first-order estimate, it misses parts of the physics involved, including radially varying gravity, the finite radial extent of the mantle, and the counterbalancing buoyancy effects of liberated hydrogen rising to shallower depths (Schiebe et al. (2021)). To quantify the energy involved, we replicated the calculation reported by Benedetti et al. (1999), who compared gravitational energies derived from a three-layer planetary model of Neptune before and after methane dissociation and redistribution.

The method begins by describing Neptune's interior structure following Hubbard (1991). In this model, the planet consists of a rocky core overlain by a molecular "ice" layer comprising primarily water, ammonia, and methane, and an outer envelope of hydrogen and helium. The total mass of Neptune's ice mantle is approximately 6×10^{25} kg. The methane fraction is estimated at about 15% by mass, yielding a total methane mass of roughly 9×10^{24} kg.

Considering the stoichiometry of methane, about 75% of this mass corresponds to carbon, giving a mass of sequestered carbon of approximately 6.8×10^{24} kg (Hubbard et. al., 1991). This carbon is assumed to precipitate as diamond and sink toward the base of the mantle during differentiation, while the accompanying hydrogen migrates toward the top of the ice layer.

The gravitational potential energy U of the planet is defined as

$$U = -\int_0^R \frac{Gm(r)dm}{r}$$

where G is the gravitational constant, m(r) is the mass interior to radius r, and dm is the mass of each spherical shell. Benedetti et al.(1999) Used two configurations to compute this integral numerically, both presented by Hubbard (1991). The first configuration represents the undifferentiated state in which the methane is uniformly distributed within the ice layer. The second configuration models the differentiated state where all the carbon has been relocated to the bottom of the ice mantle and all the hydrogen has been relocated to the top. This redistribution increases the radial concentration of mass, effectively lowering the total gravitational potential energy. The energy released is the difference in gravitational potential energy between these two configurations:

$$\Delta U = U_{differentiated} - U_{undifferentiated}$$

Because gravitational potential energy is negative by convention, this difference yields a positive value, corresponding to the energy liberated during differentiation. To approximate this integral in a more tractable form, we can express the change in gravitational potential energy of the carbon mass as the work performed by gravity in transporting the carbon mass from its initial mean radius $r_{initial}$ in the ice mantle to its final radius near the core-mantle boundary r_{final} . Neglecting the smaller contribution of hydrogen uplift, this can be approximated as:

$$\Delta U \approx GM_C M_{enc}\left(\frac{1}{r_{final}} - \frac{1}{r_{initial}}\right)$$

where M_C is the mass of carbon, and M_{enc} is the mass interior to the ice mantle (predominantly the rocky core and lower mantle). In Neptune, M_{enc} is of order 5×10^{25} kg. Taking characteristic values of $r_{initial} = 2.0 \times 10^7$ m (the mid-mantle radius), and $r_{final} = 1.0 \times 10^7$ m (near the core boundary, Hubbard (1991)), the factor in parentheses becomes:

$$\frac{1}{r_{final}} - \frac{1}{r_{initial}} = \frac{1}{1 * 10^7 m} - \frac{1}{2 * 10^7 m} = (1 - 0.5) * 10^{-7}\, m^{-1} = 5 * 10^{-8}\, m^{-1}$$

Substituting the numerical values gives:

$$\Delta U = \left(6.67 * 10^{-11} \frac{N\, m^2}{kg^2}\right)(6.8 * 10^{24}\, kg)(5 * 10^{25}\, kg)(5 * 10^{-8}\, m^{-1})$$

Evaluating these yields:

$$\Delta U = \left(6.67 * 10^{-11} \frac{N\, m^2}{kg^2}\right)(3.4 * 10^{50}\, kg^2)(5 * 10^{-8}\, m^{-1}) =$$

$$\left(6.67 * 10^{-11} \frac{N\, m^2}{kg^2}\right)\left(1.7 * 10^{43} \frac{kg^2}{m}\right) = 1.1 * 10^{33}\, J$$

This value matches the estimate reported by Benedetti et al. (1999), confirming the internal consistency of our approaches. It also demonstrates that this energy release is comparable to the total thermal output of Neptune integrated over the age of the Solar System, which is estimated at approximately 4.5×10^{32} J (Pearl et al., 1990).

Such a reservoir of gravitational potential energy underscores the potential significance of diamond sedimentation in modulating planetary thermal evolution and internal dynamics. The good agreement between this layered planetary calculation and simpler slab approximations supports the plausibility of gravitational differentiation as a process capable of contributing meaningfully to the observed energy budgets of ice giant planets.